

**POLYTECHNIC OF TURIN**

**Master's Degree in Aerospace Engineering**



**Master's Degree Thesis**

**Implementation of Non-linearity on  
Experimental Bench Transmission for  
Electro-Mechanical Controls**

**Prof. DALLA VEDOVA Matteo D. L.**

**Candidate**

**Ing. BERTONE Matteo**

**Gianluca Ciro MOSCA**

**March 2024**

## **Abstract**

Electric drive systems are essential in various industries, and ensuring their trouble-free operation is crucial. Failure to analyze the behaviors in these systems can lead to significant failures, including accidents and fatalities, as exemplified by incidents in power plants and with electric submersible pumps.

Experimental testing on actual systems is one approach, but it can be impractical due to various constraints. Therefore, mathematical models are often used to study system behavior.

Mathematical models pertaining to mechanical objects, like transmission shafts, are typically described by sets of partial differential equations, which can be challenging to solve analytically and numerically. Linear models or linearization techniques are commonly used due to the complexity of nonlinear equations. Transmission shafts, being integral components of mechanical power transmission systems, are subject to stress and oscillations, which are analyzed using various analytical methods described in existing literature [1].

The thesis proposes an approach to modeling the transmission shaft of an electromechanical actuator, which represents a promising implementation technology in the aerospace sector. This method involves developing a non-linear model capable of accurately representing the stationary operational conditions of a servomechanical actuator. The approach aims to achieve high conformity with physical objects and experimental tests while minimizing computation time, making it valuable to planning maintenance.





# Table of Contents

<b>List of Tables</b>	VII
<b>List of Figures</b>	VIII
<b>1 Introduction</b>	1
1.1 Electric Actuation Technology . . . . .	2
1.2 Prognostic . . . . .	5
1.2.1 Data-driven methodologies . . . . .	6
1.2.2 Approaches based on models . . . . .	6
<b>2 Model Representation</b>	8
2.1 Information Flow . . . . .	9
2.2 Electromechanical actuator model . . . . .	10
2.2.1 Command Module . . . . .	10
2.2.2 Resistive Load Module . . . . .	11
2.2.3 Resolver Block . . . . .	13
2.2.4 Dynamic Model of Motor Transmission . . . . .	14

2.2.5	Subsystem for Signal Acquisition . . . . .	16
<b>3</b>	<b>Experimental Test Bench</b>	<b>17</b>
3.1	Actuator Assembly . . . . .	19
3.1.1	SIMATIC Microbox PC . . . . .	20
3.1.2	SINAMICS Control Unit . . . . .	21
3.1.3	SINAMICS Power Module . . . . .	23
3.1.4	SIMOTICS Synchronous Motor . . . . .	25
3.1.5	Wolfrom Gearbox . . . . .	28
3.1.6	Encoder . . . . .	31
3.2	Servo Brake . . . . .	34
<b>4</b>	<b>Design of the Load Module</b>	<b>36</b>
4.1	Load Module Architecture . . . . .	37
4.2	Traction Springs Design . . . . .	38
4.3	Horizontal Mover . . . . .	43
4.4	Vertical Pulleys System . . . . .	44
4.5	Winding guide . . . . .	49
4.6	Data acquisition system . . . . .	50
<b>5</b>	<b>Activity Description</b>	<b>52</b>
5.1	Experimental Tests . . . . .	52
5.2	Data plotting . . . . .	53
5.3	Computation of the compliance . . . . .	59

5.4	Implementing the model . . . . .	61
<b>6</b>	<b>Results &amp; Conclusions</b>	<b>63</b>
6.1	Results . . . . .	63
6.2	Conclusion . . . . .	65
6.3	Future Developments . . . . .	66
	<b>Bibliography</b>	<b>67</b>



# List of Tables

1.1	FMECA for Electric Actuators . . . . .	4
3.1	Microbox PC technical specifications [5] . . . . .	21
3.2	SINAMICS Control Unit technical specifications [6] . .	23
3.3	SINAMICS Power Module technical specifications [7] .	25
3.4	SIMOTICS motor technical specifications [8] . . . . .	28
3.5	Number of Teeth for Gears . . . . .	30
3.6	Gearbox Technical Specifications . . . . .	31
3.7	Encoder Technical Specifications [9] . . . . .	33
5.1	Motor and Encoder final positions for every test . . . .	60

# List of Figures

1.1	EMA currently in use . . . . .	5
2.1	High-level model overview . . . . .	10
2.2	Directive Module . . . . .	10
2.3	Resistive Load module . . . . .	11
2.4	PID Control block . . . . .	11
2.5	PID Control architecture . . . . .	12
2.6	Resolver . . . . .	13
2.7	Subsystem for Dynamic Motor-Transmission Model . .	14
2.8	Borello Friction Model . . . . .	15
2.9	Signal Acquisition Subsystem . . . . .	16
3.1	Image of the experimental setup . . . . .	17
3.2	Diagram of the experimental setup . . . . .	18
3.3	Actuator assembly . . . . .	19
3.4	SIMATIC IPC427E Microbox PC . . . . .	20
3.5	SINAMICS CU310-2 PN control unit . . . . .	22

3.6	SINAMICS PM240-2 Power Module . . . . .	24
3.7	Electrical diagram . . . . .	24
3.8	SIMOTICS Synchronous Motor . . . . .	26
3.9	SIMOTICS S-1FK7 motor characteristics . . . . .	26
3.10	Pictures of the Planetary Gearbox . . . . .	29
3.11	Section of the Gearbox: Input Shaft (red), Planetary Gear (green), Output Ring (blue), Mounting Ring (gray)	29
3.12	Gearbox Geometry Layout . . . . .	30
3.13	TSW581HS Encoder . . . . .	32
3.14	Movable Stand . . . . .	32
3.15	Encoder-Gearbox Assembly . . . . .	34
4.1	Load module architecture . . . . .	38
4.2	Coil section forces . . . . .	39
4.3	D-d relation . . . . .	42
4.4	Number of coils . . . . .	42
4.5	Horizontal mover architecture (CAD) . . . . .	44
4.6	Forces on oblique pulley support (CAD) . . . . .	45
4.7	Vertical pulley system (CAD) . . . . .	46
4.8	C-support (CAD) . . . . .	48
4.9	Sliding support (CAD) . . . . .	48
4.10	Pulley (CAD) . . . . .	48
4.11	Guide (CAD) . . . . .	49

4.12	Data acquisition architecture . . . . .	50
4.13	Data acquisition hardware . . . . .	51
5.1	Data Handling (510g load) . . . . .	54
5.2	Data Handling (1000g load) . . . . .	54
5.3	Data Handling (1510g load) . . . . .	55
5.4	Data Handling (2010g load) . . . . .	55
5.5	Data Handling (2520g load) . . . . .	56
5.6	Data Handling (3020g load) . . . . .	56
5.7	Data Handling (3533g load) . . . . .	57
5.8	Data Handling (4031g load) . . . . .	57
5.9	Data Handling (4541g load) . . . . .	58
5.10	Data Handling (5042g load) . . . . .	58
5.11	Angular loss for various load levels . . . . .	61
5.12	Nonlinear model of the losses of the transmission line . . . . .	62
5.13	Model Integration . . . . .	62
6.1	Comparison of Motor positions between test bench measurements (yellow) and model computations (blue) . . . . .	64
6.2	Comparison of Encoder positions between test bench measurements (yellow) and model computations (blue) . . . . .	64



# Chapter 1

## Introduction

The aviation sector is increasingly adopting electric actuation systems, replacing traditional hydraulic ones. This shift offers significant benefits, such as reducing aircraft weight, enhancing fuel efficiency, and improving overall performance [2]. Electric systems also boast higher operational efficiency, increased design flexibility, and reduced maintenance costs. Additionally, they contribute to a quieter aircraft environment, benefiting passengers and crew.

Notably, electric actuation promises substantial weight and fuel savings, especially in aircraft like the Airbus A300 series. Cost-wise, studies show potential per-flight savings by embracing electric systems [3]. However, despite these advantages, Electric Mechanical Actuators (EMAs) still lack comprehensive understanding compared to traditional actuators, necessitating improved fault detection and prognosis, particularly in aerospace applications.

In summary, transitioning to electric actuation in aviation offers numerous benefits, including weight reduction, efficiency improvements, and cost savings. Yet, addressing challenges like fault detection remains crucial for ensuring the reliability of electric systems, especially in safety-critical aviation environments.

## 1.1 Electric Actuation Technology

Electric actuation technology typically comprises an assembly consisting of an electric motor, a power converter, and control apparatus. Integrating power conversion systems is essential because the motor's output shaft rotates at speeds ranging from thousands to tens of thousands of revolutions per minute, with limited torque. This characteristic arises because the motor's external dimensions are closely linked to torque output, while rotational speed remains relatively independent.

To address this challenge, gearboxes are commonly employed to meet torque requirements while maintaining consistent power output. This architectural configuration effectively reduces the initially high angular speed at the motor's output to a more practical range, such as 50-60 degrees per second for primary flight controls and 5-6 degrees per second for secondary controls, ensuring optimal functionality.

Electric actuators are broadly categorized into two types:

1. **Linear Electric Actuators (LEAs)**: These devices convert rotary motion into linear motion, similar to hydraulic pistons.
2. **Rotary Electric Actuators (REAs)**: These actuators produce rotary output, typically achieved by combining the motor with a mechanical gearbox.

In the conversion of rotary motion into linear motion, screw-nut couplings are commonly utilized. However, sliding screw solutions are infrequently employed in aerospace due to potential drawbacks such as increased friction and wear effects, leading to coupling degradation, backlash, and system instability. As an alternative, recirculating ball systems, where small balls move within a circular helical track, are widely adopted to minimize friction.

Despite their prevalence, recirculating ball systems face challenges like ball jamming and slippage. To mitigate these issues, especially with

small sphere diameters, roller solutions are preferred. Roller mechanisms offer enhanced load transfer capacity and enable very high transmission ratios, simplifying system complexity.

Electric actuation seamlessly integrates into fly-by-wire architecture, minimizing power conversions and component count. In this system, the pilot's command prompts Actuator Control Electronics (ACE) to generate an error signal by comparing it with input from a Linear Variable Displacement Transducer (LVDT). The LVDT provides real-time positional information, enhancing adaptability to varying loads and control conditions. The error signal, after amplification and noise filtering, regulates the system, transmitted to Power Drive Electronics (PDE), which adjusts power to the motor based on feedback and command.

Presently, electric actuators find primary usage in non-safety-critical functions, including spoilers, horizontal stabilizer trim, and high lift devices on aircraft like the Boeing 787 Dreamliner, and in the steering system for the nose wheel on the F-16 Fighting Falcon. However, broader implementation in safety-critical roles awaits advancements to address associated complexities and potential failure modes.

A Failure Modes, Effects, and Criticality Analysis (FMECA) study on electric actuator systems identified key failure modes and their occurrence rates. Notable findings include bearing wear, position sensor loss, breakdown of stator assembly insulation, and electrical open in power connectors.

<b>Component</b>	<b>Failure Rate (<math>h^{-1}</math>)</b>	<b>Failure Mode</b>
Bearings	$1.78 \times 10^{-5}$	Increased friction due to bearing wear and galling
Position sensor	$1.70 \times 10^{-5}$	Loss/incorrect feedback signal from resolver, including turn-to-turn short, turn-to-ground short, and open circuit
Brushless DC motor	$1.03 \times 10^{-5}$	Breakdown of stator assembly insulation due to turn-to-turn short, phase-to-phase short, turn-to-ground short, and open circuit
Power connector	$6.64 \times 10^{-7}$	Electrical open due to open pin or open lead-wire

**Table 1.1:** FMECA for Electric Actuators

This analysis helps in understanding the failure modes of electric actuator systems, aiding in the development of effective maintenance and reliability strategies. Additionally, ongoing research focuses on enhancing the reliability and robustness of electric actuation systems for broader integration into safety-critical aviation applications.

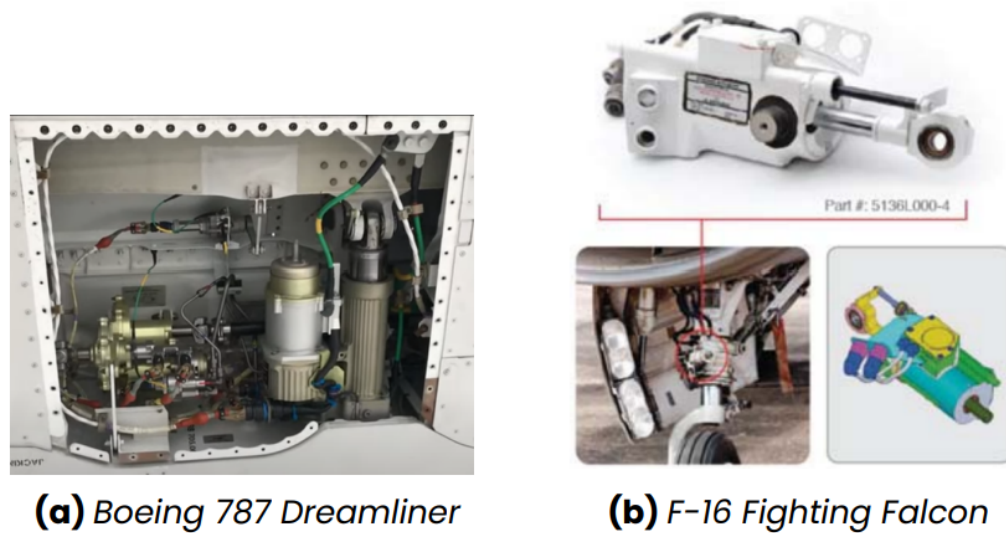


**Figure 1.1:** EMA currently in use

## 1.2 Prognostic

*Prognosis may be understood as the generation of long-term predictions describing the evolution in time of a particular signal of interest or condition indicator, with the purpose of estimating the remaining useful life (RUL) of a failing component/subsystem [4].*

Across various engineering sectors, particularly in aerospace, predictive health management (PHM) has emerged as a promising methodology for overseeing the safety, maintenance, and costs of complex systems. PHM has demonstrated the potential to significantly enhance operational and support costs (O&S), as well as the total life cycle cost of ownership (TOC), while simultaneously optimizing system availability. It facilitates the safe operation of diverse systems by continuously assessing and estimating the system's health over time, enabling optimal maintenance scheduling.

However, one of the most significant challenges in prediction lies in addressing the inherent "large-grain" uncertainty involved in forecasting

future behavior. Predicting faults in the long term, up to the verge of potential failure, requires the ability to articulate and manage this intrinsic uncertainty adeptly. Addressing such uncertainty is crucial for accurate and reliable forecasts in the domain of predictive health management.

The approach to the challenge of predictive maintenance can be broadly divided into two main factions: data-driven and model-based. Each of these approaches comes with its own set of advantages and limitations. Consequently, a common practice involves integrating both approaches, leveraging the strengths of each to achieve a more comprehensive and effective predictive solution. This integrated approach aims to harness the best features offered by both data-driven and model-based methodologies.

### **1.2.1 Data-driven methodologies**

Data-driven methodologies are rooted in the continuous monitoring of systems, using operational data to understand their behavior. These approaches rely on actual input/output metrics and statistical analysis to identify patterns associated with system faults. They excel at distilling complex, noisy data into meaningful insights, providing a deeper understanding of system conditions. However, their effectiveness is highly dependent on the availability and quality of operational data.

### **1.2.2 Approaches based on models**

Model-based approaches involve the creation of detailed mathematical frameworks to analyze system dynamics and behavior. These methods rely on comparing real-world system measurements with predictions generated by mathematical models. The underlying assumption is that significant differences between actual and predicted values, termed

residuals, indicate the presence of faults or anomalies within the system. Conversely, under normal operating conditions, where noise and modeling errors predominate, residuals are expected to be minimal.

One of the key advantages of model-based approaches is their ability to incorporate knowledge of the underlying physical principles governing the system's behavior. This allows for the development of models that accurately represent the system's dynamics and responses to various inputs. Additionally, model-based techniques offer the flexibility to adapt and refine the model as new insights into system degradation mechanisms are gained.

However, model-based approaches also come with challenges, particularly in dealing with the complexity of the mathematical models required. The intricacy of the model depends significantly on the complexity of the system under study and the accuracy required for fault detection and diagnosis. Managing this complexity while ensuring the model remains tractable and computationally efficient is a key consideration in model-based prognostic methods.

## Chapter 2

# Model Representation

To develop an algorithm capable of recognizing anomalies in electromechanical actuators, it is crucial to construct a computational model that accurately mirrors the real-world behavior of the components. A key focus has been placed on mimicking the reaction time of a system positioned between primary and secondary flight controls.

With this aim in mind, the model implemented in Matlab-Simulink adopts a fine-grained integration step of  $1 \times 10^{-6}$  seconds. This decision enables accurate representation of the electronic component's behavior while staying significantly below the characteristic time of the electronic side, typically by one or two orders of magnitude.

Given the necessity to simulate the system's behavior over extended temporal spans, a fixed-step integration approach has been employed. Specifically, ODE 1, known as Euler's method, has been opted for. While this preference places additional demands on computational resources, it offers a more streamlined memory utilization, essential for accurately modeling the system over prolonged periods.

## **2.1 Information Flow**

The complete system embodies a position-regulated actuator, wherein the output of the "Communication" block signifies a positional indication directed towards the "Control system" subsystem. This subsystem simulates the behavior of the actuator's control system, generating a current intensity regulated by the deviation between the instructed and actual positions of the actuator, alongside the actual motor velocity. The resultant output from this element is then routed to the "Inverter emulation" subsystem.

Within the inverter subsystem, which collaborates with the "Electromagnetic emulation" subsystem, supply voltages for the motor's distinct phases are generated by incorporating the position provided by the "Resolver emulation" subsystem. The "Electromagnetic emulation" subsystem facilitates the evaluation of currents flowing in various motor phases, considering the influence of motor transmission dynamics. These dynamics stem from the "Motor transmission dynamics emulation" subsystem, where external resistive forces and propelling forces impact the position and angular velocity of the motor-gearbox assembly.

The concluding element, the "Data Acquisition" subsystem, provides direct current and quadrature current values derived from the currents circulating in each of the three phases.

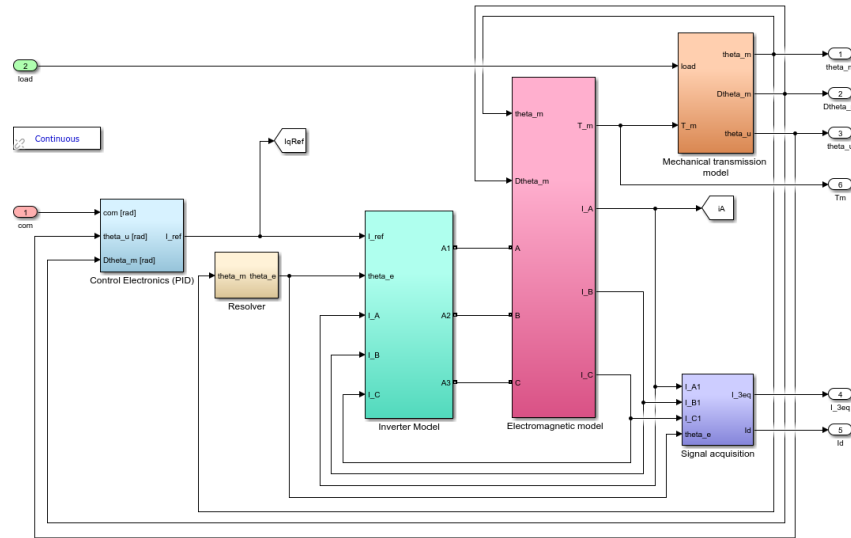


Figure 2.1: High-level model overview

## 2.2 Electromechanical actuator model

### 2.2.1 Command Module

The "Com" module offers the capability to specify the type of positional directives to validate the model. It enables the creation of directives

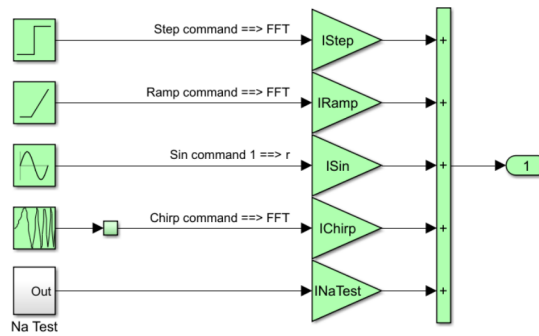


Figure 2.2: Directive Module

such as step, ramp, sinusoidal wave, or chirp, and also allows for their combination. This broad spectrum of directives enables the simulation

of a diverse range of operational scenarios for the modeled physical component.

### 2.2.2 Resistive Load Module

The "Load" module applies resistance to the model. This component



**Figure 2.3:** Resistive Load module

is realized through the utilization of a pure step function, effectively simulating the static conditions under which our analysis is conducted.

### PID Control Architecture

The “PID” block is composed of three distinct branches: proportional (P), integral (I), and derivative (D).

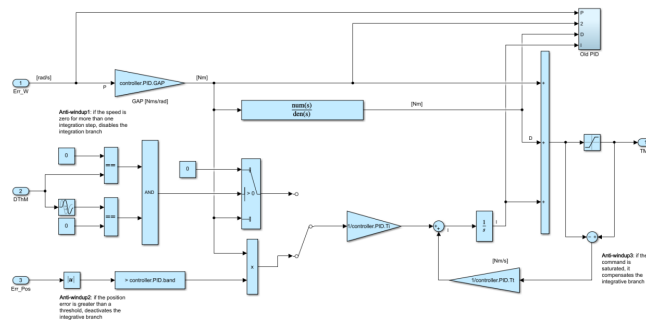


**Figure 2.4:** PID Control block

It can be described as the application of a transfer function

$$f(s) = \frac{T_d s}{\frac{T_d}{N} s + 1}$$

where  $T_d$  represents the time constant of the derivative branch, and  $N$  is the derivative filter bandwidth.

This branch helps mitigate noise amplification compared to numerical differentiation methods, thus reducing the number of components required in the system.

However, it's important to note that this transfer function specifically addresses the derivative action within the PID controller, rather than the entire PID control architecture.

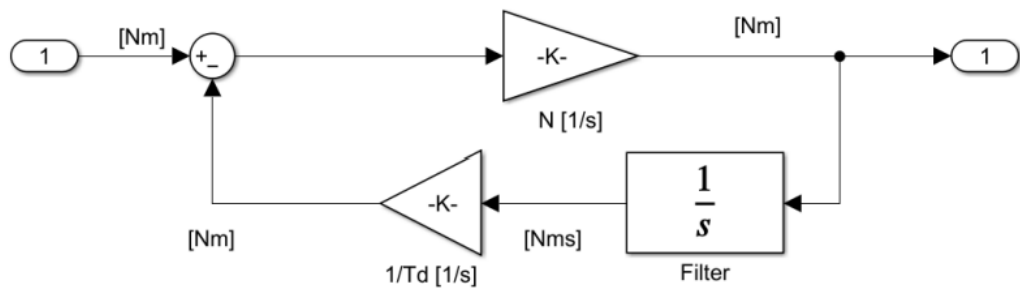


**Figure 2.5:** PID Control architecture

The integral branch computes a signal associated with the integral of the position error. While crucial, this branch can lead to windup—a scenario where system saturations prevent the attainment of the desired signal value. The model introduces three anti-windup strategies:

- **Anti-windup 1:** Analyzes motor velocity, deactivating the integral branch if the speed remains zero for more than one integration step.
- **Anti-windup 2:** Evaluates position error, deactivating the integral branch if the error exceeds a predetermined threshold.

- **Anti-windup 3:** Compares the error between the ideal and saturated output signal. During saturation, the difference generates an error which, when multiplied by the integral branch gain, diminishes its contribution.

The third solution demonstrates greater efficacy during simulations, as the first two possess inherent limitations. The first strategy may deactivate the integral branch during critical conditions, while the second is confined by the necessity to predefine the threshold value.

The PID block’s summation of torques from the proportional, integral, and derivative branches serves as the motor’s reference torque.

### 2.2.3 Resolver Block

The “Resolver” block facilitates the derivation of the electrical angular position based on the known mechanical angular position.

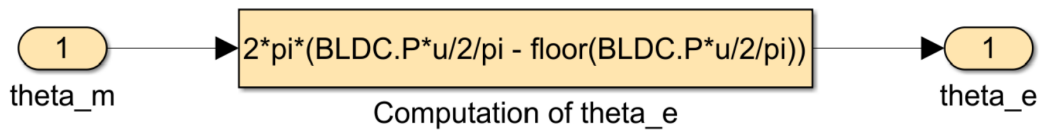


**Figure 2.6:** Resolver

The electrical angular position is correlated with the mechanical position through the number of motor poles pairs. The general expression is given by:

$$\theta_e = N_p \theta_m$$

where:

- $\theta_e$ : Electrical angular position
- $N_p$ : Mechanical angular position
- $\theta_m$ : Motor poles pair

In this specific model, the formula used is slightly more intricate as it imposes a constraint on the possible output values of the position, limiting them to the range of 0 to  $2\pi$ .

### 2.2.4 Dynamic Model of Motor Transmission

Within this subsystem, the interaction between the motor-generated torque and resisting torques is simulated to analyze the kinematic parameters of the motor-transmission setup.

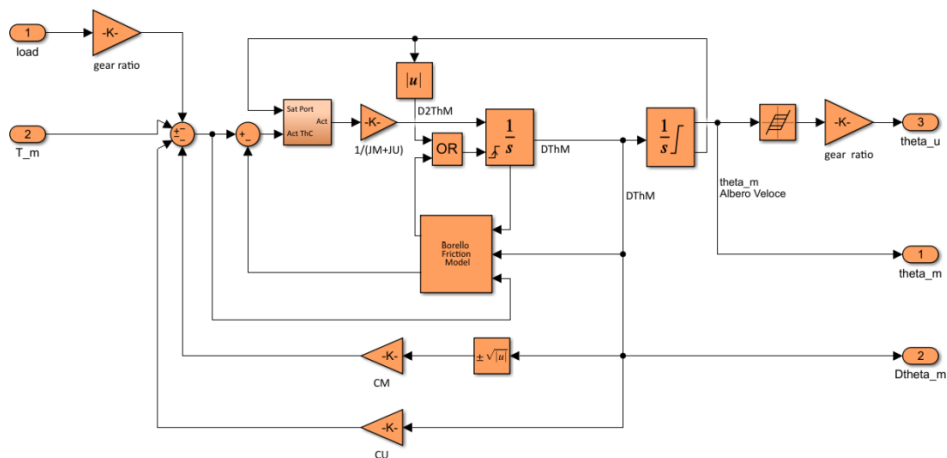


**Figure 2.7:** Subsystem for Dynamic Motor-Transmission Model

To accurately model dynamic behavior, torques are initially referred to the same shaft, particularly the fast one. Additionally, estimation of the viscous resistance component is crucial. This is achieved by multiplying the motor's angular velocity by a viscous damping coefficient, representing the system's overall viscous behavior. The residual torque affecting the system, along with the rotational speed at different integration steps, is then fed into the "Borello Friction Model" block to emulate friction effects. The Borello friction model is preferred for its accuracy and simplicity in reproducing critical system behaviors, enabling precise differentiation between static and dynamic friction conditions.

The "Borello Friction Model" block is bifurcated into two primary branches, one for assessing dynamic friction and the other for static friction. The discriminating factor between activating one branch or the other is the velocity at the current integration step. If the velocity crosses the zero mark, the branch handling static friction is triggered, and simultaneously, the integration block's velocity is reset to zero. This allows for the verification of static friction conditions. If the static friction forces surpass those generated by the motor, the system will maintain its current position. Conversely, if the motor's forces exceed static friction, the system will resume motion, subject again to dynamic friction.

Furthermore, this subsystem replicates the effects of mechanical limit stops. This is achieved through a signal flag from the integrator responsible for position determination. The saturated integrator restricts the output position value and generates a signal flag to indicate its status (upper limit exceeded, not limited, lower limit exceeded). This signal flag is then utilized to override velocity and determine the resultant constraint reactions.

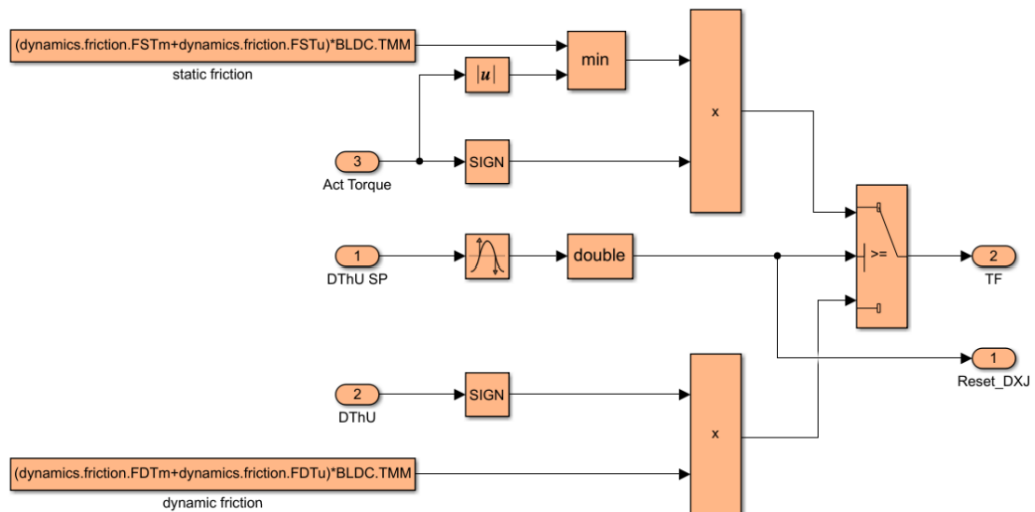
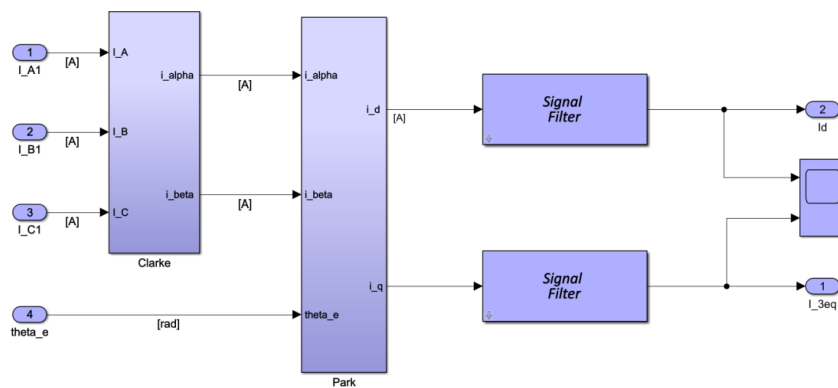


Figure 2.8: Borello Friction Model

Finally, backlash effects are reproduced within this subsystem. A specialized block is introduced to limit the output in case the input value changes direction.

## 2.2.5 Subsystem for Signal Acquisition

The "Signal Acquisition" subsystem facilitates the retrieval of direct and quadrature currents based on the individual phase currents and the electrical position of the motor.



**Figure 2.9:** Signal Acquisition Subsystem

Its functionality resembles the subsystem responsible for assessing phase currents within the "Inverter model". However, in this case, the direct Clark-Park transformation is employed instead of the inverse transformation.

## Chapter 3

# Experimental Test Bench

In order to validate and ensure the precise functionality of the model discussed in the previous section, an experimental setup has been carefully devised. This setup serves as a real-world counterpart for validating and cross-referencing the results obtained from simulations.

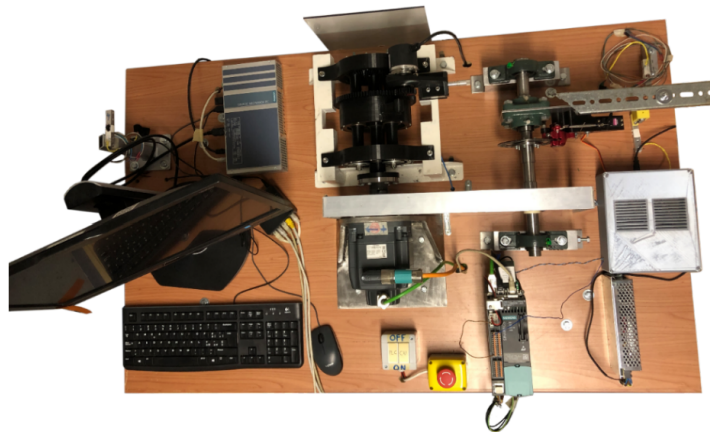


**Figure 3.1:** Image of the experimental setup

The experimental setup can be broken down into two main parts: the actuation module and the resistive load generation module. The actuation module, which carries out commands, consists of a motor-gearbox assembly along with the necessary control and power electronics. On the other hand, the resistive load generation module includes a shaft housing a brake, controlled by an electronic controller to regulate the applied resistive load. A chain sprocket transmission links these two modules. It's worth noting that the components within the actuation module, except for the transmission, are obtained from industrial sources. While they share similarities in architecture and failure modes with their aerospace counterparts, these components are more easily accessible and adaptable for customized applications.

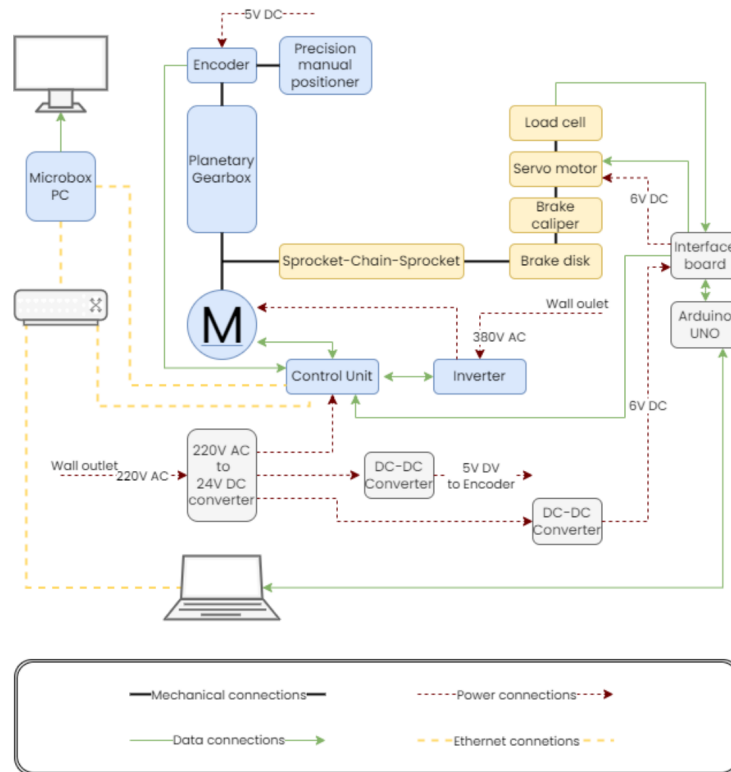


**Figure 3.2:** Diagram of the experimental setup

### **3.1 Actuator Assembly**

The actuator module primarily comprises components provided by Siemens, such as the Microbox PC, Control Unit, and Power Module, facilitating the controlled operation of the Sinamics S120 PMSM motor. The only internally developed component is the planetary gear-box linked to the motor's output shaft. The Microbox PC oversees the operation of these components, hosting the PLC responsible for high-level logic governing position command tracking. Reference positions are then transmitted to the Control Unit, tasked with driving the connected inverter to power the motor. Subsequently, the transmission is coupled to the motor's output shaft, resulting in appropriate angular speed reduction and rotation of the end-user encoder.

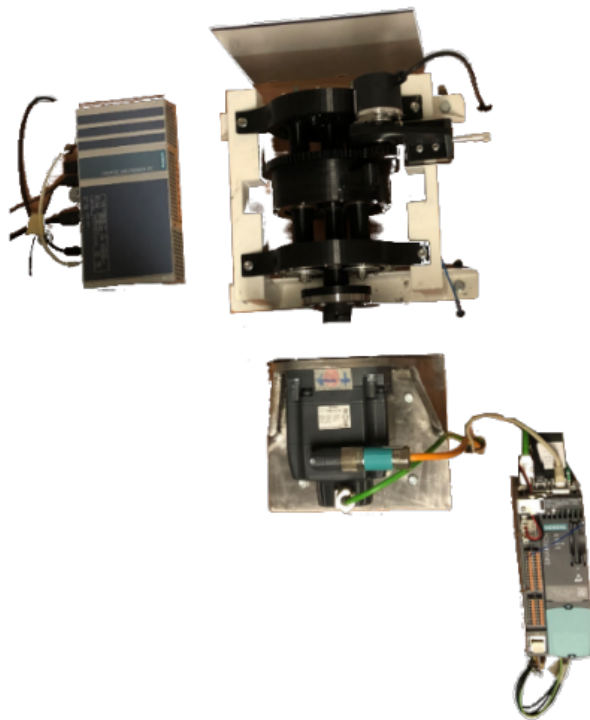


**Figure 3.3:** Actuator assembly

### 3.1.1 SIMATIC Microbox PC

The primary processing and control unit within the actuation system, composed of Siemens components, is the SIMATIC IPC427E Microbox PC.



**Figure 3.4:** SIMATIC IPC427E Microbox PC

This component is a compact PC designed for passive cooling, tailored to provide processing capabilities in close proximity to controlled machinery. It serves as an ideal platform for applications ranging from application virtualization to data acquisition and analysis.

In the adopted architecture, its role is to virtualize the PLC and host the server necessary for command management. This control server, accessible via a web portal, offers expanded control capabilities. With specialized compilers, it allows for the creation of more complex control logic in the Matlab language compared to what is achievable at the PLC level.

Installation type	DIN rail, wall mounting
Power supply	24V DC (max 4A)
Processor	Intel Core i3-6102E
Memory	16 Gbyte DDR4-SDRAM SO-DIMM
Storage	128 Gbyte SATA SSD
Interfaces	3x industrial Ethernet (RJ45), 4x USB port (USB 3.0), 2x serial COM (RS 232/485/422), 2x display ports
IP degree of protection	IP20
Ambient temperature during operation	0°C to 55°C
Dimensions	Width 262 mm, Height 139.7 mm, Depth 55.5 mm

**Table 3.1:** Microbox PC technical specifications [5]

### 3.1.2 SINAMICS Control Unit

The SINAMICS Control Unit (CU310-2 PN) is a crucial component in the actuator assembly, responsible for processing and controlling the Sinamics S120 PMSM motor.

Directly connected to the power supply unit, it interfaces with the power unit and various peripherals for sensor integration. In the adopted architecture, the CU310-2 PN connects to the PLC and motor encoder via Ethernet, while also receiving data from the gearbox encoder through a serial interface.

Equipped with autonomous operation capabilities, the CU310-2 PN can host custom firmware on a memory card, ensuring functionality even without constant communication with the PLC. This autonomy is valuable for scenarios requiring continuous motor control. The control unit supports both open-loop and closed-loop motor speed control,

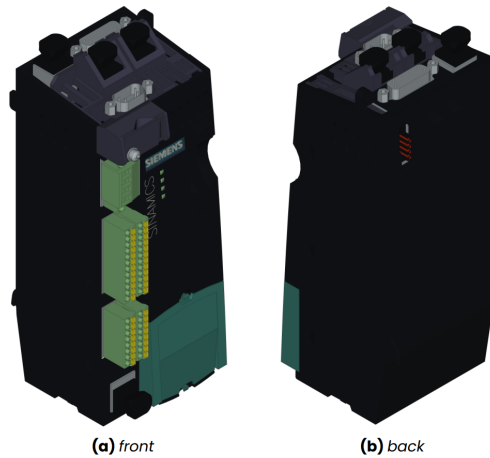


**Figure 3.5:** SINAMICS CU310-2 PN control unit

offering flexibility for different operational requirements. Its standardized 24V DC power supply aligns with the overall system design, simplifying power management across control components.

In summary, the SINAMICS CU310-2 PN control unit plays a pivotal role in the actuator assembly, providing essential processing and control capabilities for efficient and precise control of the Sinamics S120 PMSM motor in diverse industrial applications.

Power supply	24V DC (max 0.8A)
Interfaces	3x PROFINET <sup>1</sup> 1x DRIVE-CLIQ <sup>2</sup> 1x Ethernet/IP
Encoder interface	Incremental encoder TTL/HTL or encoder SSL without incremental signals
Encoder frequency, max	300 kHz
Number of digital Inputs	11
Number of digital I/O	8
Digital signals voltage	-3V to 30V
Digital signals low level	-3V to 5V
Digital signals high level	15V to 30V
Number of analog input	1
Ambient temperature during operation	0°C to 55°C
Dimensions	Width 73 mm Height 191 mm Depth 75 mm

**Table 3.2:** SINAMICS Control Unit technical specifications [6]

### 3.1.3 SINAMICS Power Module

The key power management component within the actuator assembly is the SINAMICS PM240-2 Power Module, as depicted in Figure 3.6. This integral module serves as an air-cooled, modular inverter operating on 380V AC. Its distinctive feature lies in the seamless integration of a diode rectifier, an inverter, and the capacity to dissipate braking currents efficiently through external resistor banks—all within a single,

---

<sup>1</sup>Real-time implementation of ethernet communication

<sup>2</sup>Siemens proprietary communication interface

compact component.

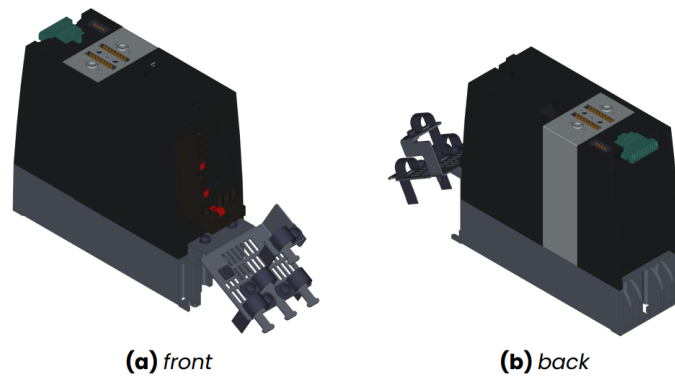


**Figure 3.6:** SINAMICS PM240-2 Power Module

The SINAMICS PM240-2 plays a pivotal role by directly interfacing with the SINAMICS CU310-2 PN, facilitating the smooth flow of power within the actuator system. Its innovative design ensures not only effective power conversion but also the ability to handle braking currents, contributing to the overall efficiency and reliability of the actuator assembly.

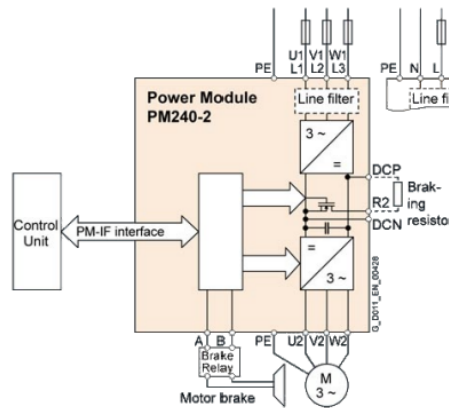


**Figure 3.7:** Electrical diagram

<b>Input</b>	
Number of phases	3 AC
Line voltage	380V to 480V
Line frequency	47 Hz to 63 Hz
Rated current	2.00 A
<b>Output</b>	
Number of phases	3 AC
Pulse frequency	4 kHz
<b>General specifications</b>	
Power factor	0.85
Efficiency	0.96
IP degree of protection	IP20
Cooling	Internal air cooling
Ambient temperature during operation	-5°C to 40°C
Net weight	1.50 kg
Dimensions	Width 73 mm Height 196 mm Depth 165 mm

**Table 3.3:** SINAMICS Power Module technical specifications [7]

### 3.1.4 SIMOTICS Synchronous Motor

The engine integrated into the test bench is a SIMOTICS S 1FK7060-2AC71-1CG0 synchronous motor, as illustrated in Figure 3.8.

The 1FK7 motors belong to the category of lightweight permanent magnet motors designed for efficient heat dissipation through the motor surface, eliminating the need for external cooling systems. This motor incorporates an absolute encoder within its structure, utilized by the CU to precisely regulate currents across individual phases.

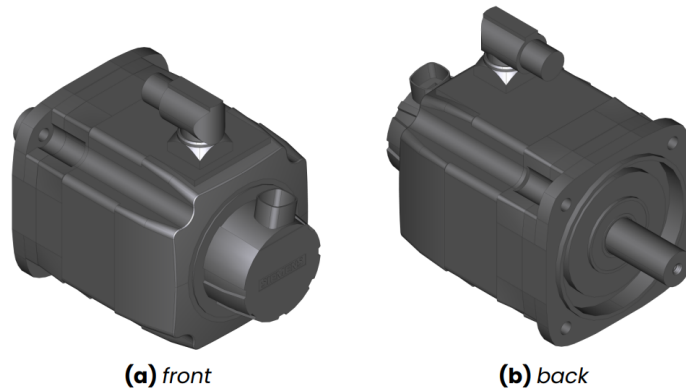


**Figure 3.8:** SIMOTICS Synchronous Motor

To ensure optimal functionality of the electrical and magnetic components, operating temperatures are deliberately limited. Consequently, the torque output is restricted and correlated with the rotational speed to maintain the motor within specified temperature thresholds.

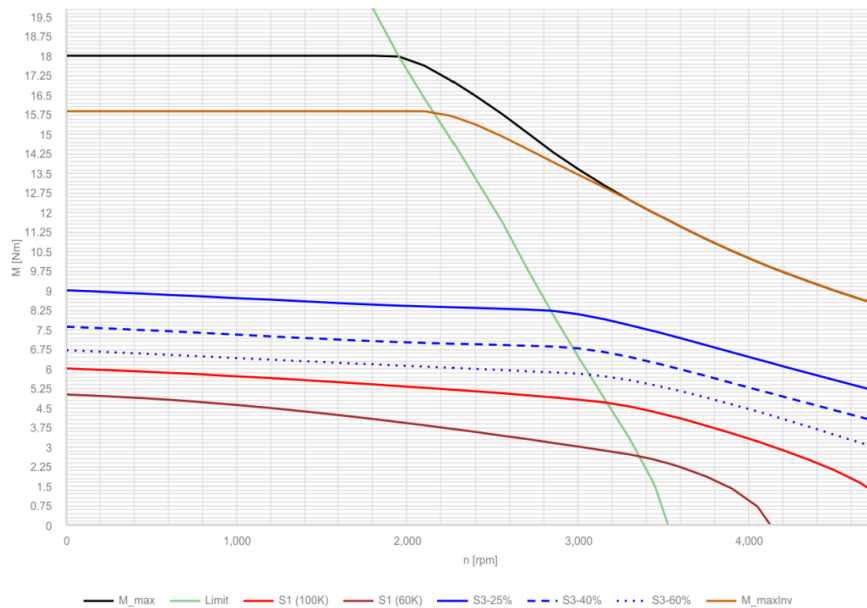


**Figure 3.9:** SIMOTICS S-1FK7 motor characteristics

Continuous operation characteristics are defined by the S1 (100K)

curve, indicating the upper limit of permitted operation at a component working temperature of 155°C. An alternative S1 (60K) curve ensures safer operation at 90°C, mitigating conditions that could adversely affect the component. Intermittent operation is detailed by S3-25%, S3-40%, and S3-60% curves, allowing higher loads based on phase activation while still adhering to the 155°C over-temperature limit. The maximum torque under any operating condition remains lower than  $M_{max}$ .

In addition to temperature-related limitations, rotational speeds face constraints arising from electrical and mechanical factors. The power electronics' ability to switch at high frequencies required for elevated rotational speeds and the motor's resistance to centrifugal forces in moving parts dictate these speed limits.

Motor type	Compact permanent-magnet synchronous motor
Number of poles	8
Rated current	3.0 A
Efficiency	0.90
Degree of protection	IP64
Cooling	Natural cooling
Temperature monitoring	Pt1000 temperature sensor
Encoder system	Encoder AM24DQI: absolute encoder 24 bits (resolution 16777216) + 12 bits multi-turn
Net weight	7.1 kg
<b>Motor characteristics</b>	
Rated speed (100K)	2000 rpm
Rated torque (100K)	5.3 Nm
Static torque (100K)	6.0 Nm
Stall current (100 K)	3.15 A
Static torque (60K)	5.0 Nm
Stall current (60K)	2.55 A

<b>Electrical and mechanical constants</b>	
Moment of inertia	7.700 kgcm <sup>3</sup>
Torque constant	1.91 Nm/A
Winding resistance at 20°C	2.75 Ω
Time constants	Thermal 30 min
	Electrical 11.10 ms
	Mechanical 1.75 ms
<b>Optimum operating point</b>	
Optimum speed	2000 rpm
Optimum power	1.1 kW
<b>Limiting data</b>	
Max. permissible speed (mech.)	7200 rpm
Max. permissible speed (inverter)	4750 rpm
Maximum torque	18 Nm
Maximum current	10.7 A

**Table 3.4:** SIMOTICS motor technical specifications [8]

### 3.1.5 Wolfrom Gearbox

Due to the high angular speeds generated by compact motors, the implementation of a gearbox becomes essential to amplify torque and reduce angular speed at the user shaft. The planetary transmission incorporated into the test bench is a high transmission ratios gearbox developed by Politecnico di Torino. Notably, it was manufactured utilizing additive manufacturing techniques, specifically Fused Deposition Modeling (FDM), ensuring rapid development and cost-effectiveness.

The gearbox's structure comprises a central input shaft surrounded by three planetary gears enclosed in a support ring. These planetary gears



**Figure 3.10:** Pictures of the Planetary Gearbox

share the shaft with secondary stage gears responsible for driving the output ring, as illustrated in Figure 3.11.

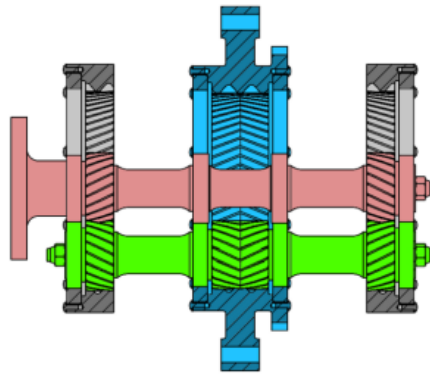


**Figure 3.11:** Section of the Gearbox: Input Shaft (red), Planetary Gear (green), Output Ring (blue), Mounting Ring (gray)

A pivotal feature of this planetary gearbox design is the mirroring of the first stage to maintain equilibrium among the forces exerted on the satellites. Consequently, a planet carrier is unnecessary, as it

experiences no applied torque or force. Another distinctive aspect is the utilization of helical teeth, adept at managing axial loads in both directions. This, coupled with a symmetrical tooth orientation, results in self-supporting planetary shafts that eliminate the need for bearings.

### Gearbox Property Determination

The geometric characteristics of the gearbox design are summarized as depicted in Figure 3.12. The number of teeth for each gear is specified in Table 3.5.

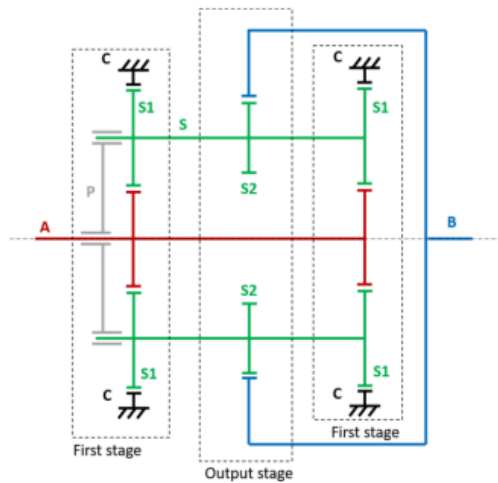


**Figure 3.12:** Gearbox Geometry Layout

$z_A$	21
$z_{S1}$	21
$z_{S2}$	20
$z_B$	62
$z_C$	63

**Table 3.5:** Number of Teeth for Gears

Willis's equation is employed to determine the overall gear ratio, offering a general relationship based on the number of teeth for each gear:

$$\tau = \frac{\omega_A}{\omega_B} = \frac{1 + \frac{Z_A}{Z_C}}{\frac{Z_A}{Z_C} - \frac{Z_A Z_{S1}}{Z_{S1} Z_B}}$$

The transmission moment of inertia is estimated by assuming unitary density and length of the structure. The moments of inertia for different components are calculated based on their geometric characteristics. The overall moment of inertia reduced to the input shaft is found to be  $1.75 \times 10^{-6} gmm^2$ .

Manufacturing Technique	FDM
Material	PLA
Reduction Ratio	124
Inertia Reduced to Input Shaft	$1.75 \times 10^{-6} gmm^2$
Max Torque	2.3 Nm
Ultimate Torque	10.8 Nm $\pm$ 10%

**Table 3.6:** Gearbox Technical Specifications

### 3.1.6 Encoder

The encoder installed on the gearbox output shaft is a high-resolution optical incremental encoder, specifically the TSW581HS model.

This encoder facilitates closed-loop position control of the motor with a resolution sufficient to observe the effects of backlash. Its optical design, composed of a light source, a spinning disk, and a photo-detector, ensures simplicity and reliability. The incremental nature of the encoder allows the determination of position changes, requiring only two output signals labeled channels A and B. These channels indicate both the position and rotation direction, utilizing two coded disks with out-of-phase sectors. Discrimination of the rotation direction is achieved

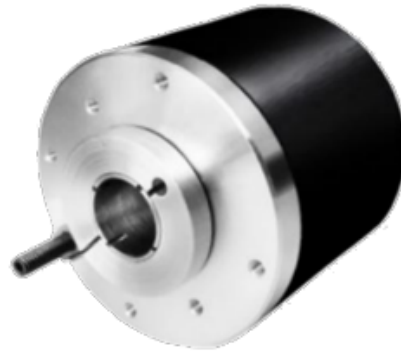


**Figure 3.13:** TSW581HS Encoder

by observing the leading signal in one of the two channels, while the position is measured by counting the signal fronts of both channels.

The characteristics of the encoder mounted on the user output are summarized in the table below.

To facilitate fine-tuning of the measured backlash, the encoder is installed on a movable stand.

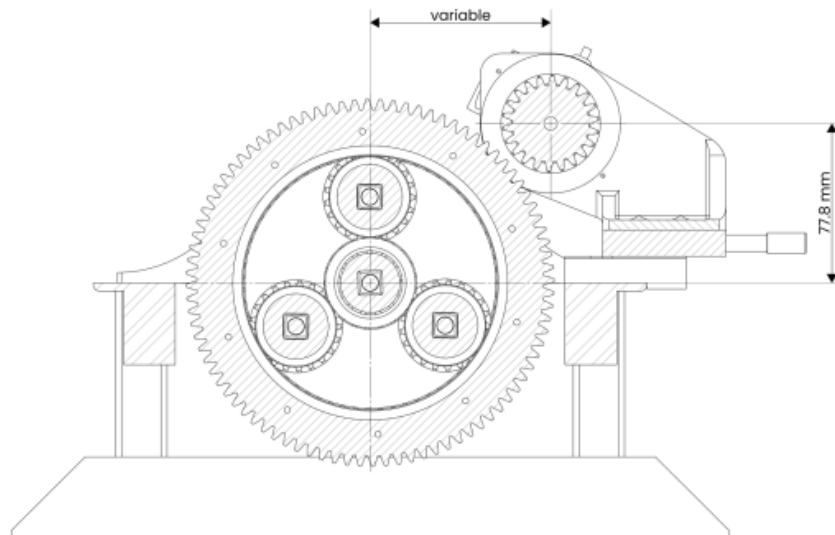


**Figure 3.14:** Movable Stand

Part Number	TSW581HS.M2.5000.5. V.K4.B127.PL10.PP2-5
Resolution	5000 ppr
Output Frequency	Up to 300 kHz
Continuous Speed	6000 rpm
Degree of Protection	IP64
Ambient Temperature During Operation	-10 °C to 70 °C
Net Weight	0.25 kg
Moment of Inertia	40 $g^2$ cm
<b>Electrical</b>	
<b>Characteristics</b>	
Power Supply	5V DC (max 150mA)
Output Circuit	Push-Pull 5V output only
Protection	Short Circuit (No Limit Du- ration)
<b>Mounting</b>	
Shaft	$\phi$ 12.7 mm
Type	Spring M2
<b>Optimum Operating</b>	
<b>Point</b>	
Flange	Aluminum
Housing	Polyamide
Shaft	Stainless Steel

**Table 3.7:** Encoder Technical Specifications [9]

The support structure consists of three main parts: the attachment element to the gearbox support structure, the micro-mover, and the angled encoder support. The attachment element serves as an adapter between the gearbox and micromover attachment systems, ensuring accurate and repeatable positioning. The micro-mover allows precise

measurement of the distance traveled by the encoder support structure. The encoder support structure has an inward angle, placing the encoder gear at a  $45^\circ$  angle to the output gear of the reduction. This orientation enhances the micro-mover's sensitivity, enabling measurement of minimal backlash.

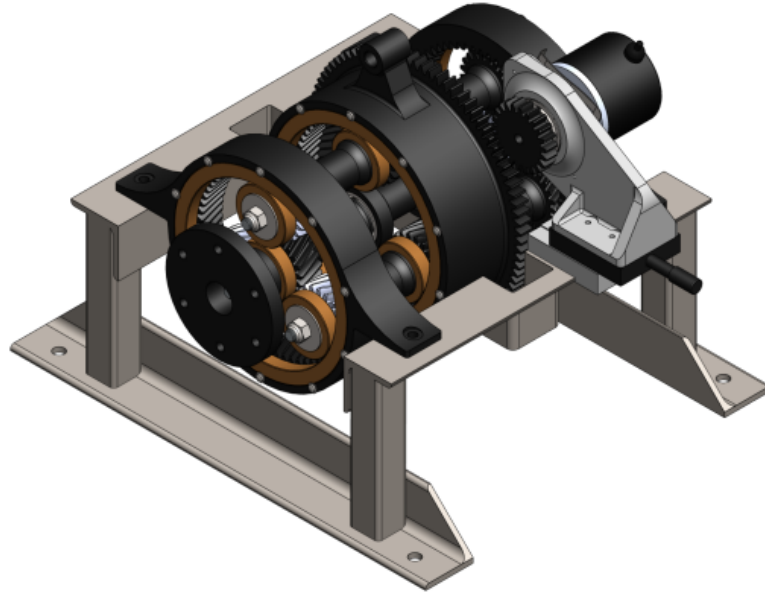


**Figure 3.15:** Encoder-Gearbox Assembly

## 3.2 Servo Brake

The test bench incorporates a servo brake designed to apply braking torque directly to the output of the electric motor, positioned before the gearbox. A disc brake is mounted on a shaft parallel to the electric motor shaft, with a chain connecting the motor shaft to the brake module shaft, enabling transmission of the braking torque.

To achieve the desired braking torque, the braking module comprises:

- **Servo Motor:** Digital Servo DM5163M

- **Arduino R3 Board**
- **Load Cell**

An Arduino-based control algorithm is utilized to attain the desired braking torque. When a braking torque command is issued, the Arduino instructs the servo motor to reach the specified position for the desired torque. Simultaneously, a load cell, integrated into the test bench and connected to the brake servo motor via a 3D-printed hinge, measures the force exerted on the table surface. By multiplying this force by the distance from the axis of the braking module, the effective braking torque is determined.

The error between the commanded braking torque and the actual braking torque is then calculated using the following equation:

$$\text{error} = \text{set} - \text{torque}$$

Here, "set" represents the commanded torque, and "torque" denotes the effective braking torque measured by the load cell.

The Arduino utilizes this calculated error as input to a control algorithm based on proportional-integral (PI) control logic, incorporating proportional and integral gains. This control logic aims to minimize the steady-state error, ensuring accurate and consistent braking performance.

## Chapter 4

# Design of the Load Module

Simulating external loads holds significant importance, especially in aeronautics, where actuators are consistently exposed to mechanical and aerodynamic loads of varying magnitudes. For instance, actuators controlling moving surfaces must continually counter aerodynamic loads transmitted from these surfaces onto the actuation system. Despite the challenges in directly measuring external loads in aeronautical applications, understanding them is invaluable for developing prognostic and diagnostic algorithms.

In this chapter, we delve into the detailed design and operation of the load module.

## 4.1 Load Module Architecture

Additive manufacturing, specifically fused deposition modeling (FDM), was employed to fabricate the mechanical components of the load module. These components were initially designed using CAD software and subsequently 3D printed.

These components comprise traction springs, a horizontal mover, vertical and oblique pulleys, a winding guide, wires, and a data acquisition system. Alternatively, weights can be used to apply a constant load depending on the actuation. Springs are useful for reproducing a load based on position, such as aerodynamic loading. The operation of the load module leverages the gearbox's rotation. Two cables are affixed to the gearbox, wrapping around a guide as the gearbox rotates. These cables are connected to two springs, which, upon the gearbox's rotation, are tensioned. The force generated by the springs pulling is transmitted via cables wrapping around transmission pulleys and ultimately discharged onto the gearbox. This mechanism effectively transmits torque to the gearbox, simulating external loads on the system.

To ensure torque application, the tension forces exerted by the cables on the gearbox must oppose each other. Hence, one cable tensions the gearbox from the top, while another tensions in the opposite direction at the bottom. This arrangement generates torque, expressed as  $M = Fd$ , where  $F$  represents the spring force transmitted by the cables to the gearbox, and  $d$  denotes the diameter of the winding guide.

Subsequently, the cables wind around a set of pulleys positioned on opposite sides of the gearbox. Vertical pulleys on the left act as guides for the cable above the gearbox, while the mover on the right directs the cable below. Both cables are then routed inside two parallel tubes placed beneath the test bench, housing the two springs. Finally, the cables are anchored to the springs. As the motor rotates, the cables

wind around the guide, and the pulleys tension the springs, thereby generating the requisite force to apply torque to the gearbox.

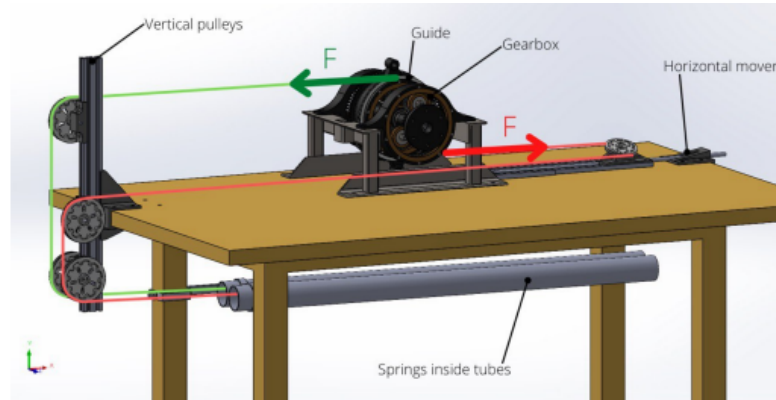


**Figure 4.1:** Load module architecture

## 4.2 Traction Springs Design

Traction springs serve as crucial components for generating torque within the system. They exert tension on the transmission cables, which in turn transfers this tension to the gearbox mounts. This mechanism, achieved by applying opposing forces spaced apart, enables the generation of the desired torque. Each cable is connected to identical springs, ensuring symmetrical tension distribution when the motor rotates. Springs are chosen due to their ability to provide a load that correlates proportionally with the motor's rotation.

The design of traction springs depends on several key parameters, including wire diameter ( $d$ ), mean coil diameter ( $D$ ), free length ( $L_0$ ), number of coils ( $n$ ), and pitch ( $p$ ).

In extension springs, it's common for the pitch ( $p$ ) to match the wire diameter ( $d$ ), resulting in tightly connected coils for a more compact spring design. Hence,  $p = d$  in such cases.

Additional design parameters need determination. The load module is engineered to apply a maximum torque ( $M_{\max} = 12 \text{ Nm}$ ) to the gearbox. Given a rail diameter ( $d_{\text{rail}} = 160 \text{ mm}$ ) around which the cables wind, each spring under maximum load should generate a tensile force:

$$F = \frac{M_{\max}}{d_{\text{rail}}} = \frac{12 \text{ Nm}}{0.16 \text{ m}} = 75 \text{ N}$$

For safety considerations,  $F$  is rounded up to 80 N.

Considering the cross-section of a coil, the force ( $F$ ) exerted on the spring can be decomposed into tangential ( $F_t$ ) and normal ( $F_n$ ) components to the wire section, as depicted in Figure 4.2.

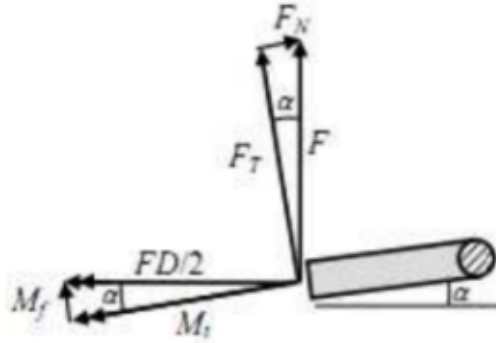


**Figure 4.2:** Coil section forces

With  $F_n = 0$  and  $M_f = 0$  assuming a sufficiently small angle  $\alpha$ , all force is absorbed in shear, simplifying to  $F_t = F$  and  $M_t = FD/2$ . The maximum shear stress ( $\tau_{\max}$ ) at the most stressed point can be calculated as:

$$\tau_{\max} = \frac{8FD}{\pi d^3} + \frac{4F}{\pi d^2}$$

The objective is to find a combination of  $D$  and  $d$  that ensures the spring remains below its yield strength, even under the most critical conditions ( $F = 80 \text{ N}$ ). Utilizing the Von Mises criterion, the shear stress ( $\tau_{\max}$ ) is related to the yield stress ( $\sigma_{0.2}$ ) of the steel composing

the spring as:

$$\tau_{\max} = \frac{\sigma_{0.2}}{\sqrt{3}}$$

resulting in the external diameter ( $D$ ):

$$D = \frac{\sigma_{0.2}\pi d^3}{8\sqrt{3}Fc} - \frac{d}{2}$$

The spring stiffness ( $K$ ) is calculated as:

$$K = \frac{Gd^4}{8nD^3}$$

where  $G$  is the shear modulus of spring steel, and  $n$  is the number of coils.

Given the known maximum force ( $F = 80$  N) and fixing the spring elongation ( $x = 1.3$  m), the required spring stiffness ( $K$ ) is calculated as:

$$K = \frac{F}{x} = \frac{80 \text{ N}}{1.3 \text{ m}} = 0.0615$$

The design parameters for the spring are determined through the following procedure:

- A value of  $d$  is chosen.
- $L_0$  is calculated as  $L_0 = nd$ .
- All design parameters ( $D, d, n, L_0$ ) are known.

A MATLAB software tool was developed based on this procedure, utilizing values from UNI EN 10270-1 SM/SH/DH as reference for yield stress and shear modulus. Input parameters include  $K = 0.0615$ ,  $F = 80$  N,  $G = 81500$  N/mm<sup>2</sup>,  $\sigma_{0.2} = 1730$  N/mm<sup>2</sup>, and a safety factor  $c = 2$ .

Wire diameter ( $d$ ) is the last input parameter to be defined. Solutions were calculated for different initial values of  $d$ , varying between 2 mm and 4 mm, yielding different mean diameters ( $D$ ). These values are illustrated in blue in Figure 4.3. The chosen design point, ensuring structural strength, consists of  $d = 3$  mm and  $D = 34$  mm.

With  $n = 342$  coils, it is calculated that the spring length ( $l_0$ ) must be:

$$l_0 = nd = 342 \times 3 \text{ mm} = 1026 \text{ mm}$$

In summary, the design parameters for the spring are:

- $d = 3$  mm
- $D = 34$  mm
- $l_0 = 1024$  mm
- $n = 342$

The springs were manufactured using UNI EN 10270-1 SM/SH/DH spring steel, also known as C72.

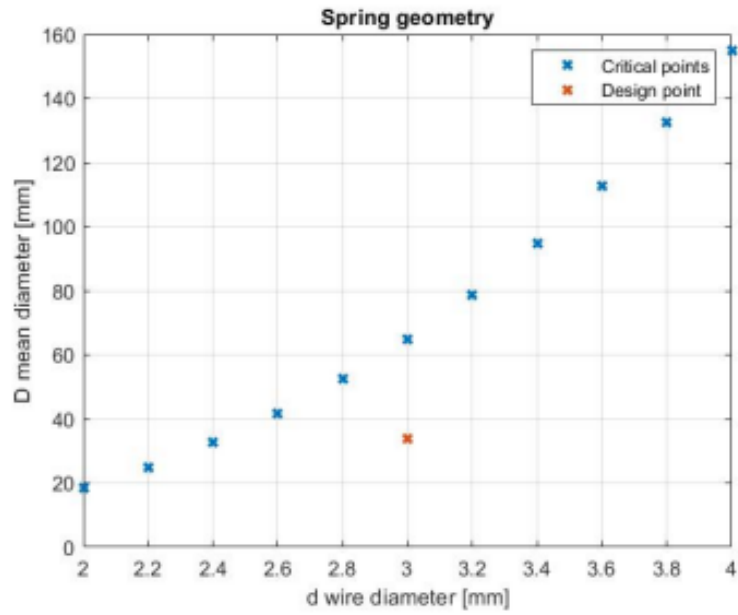


**Figure 4.3:** D-d relation

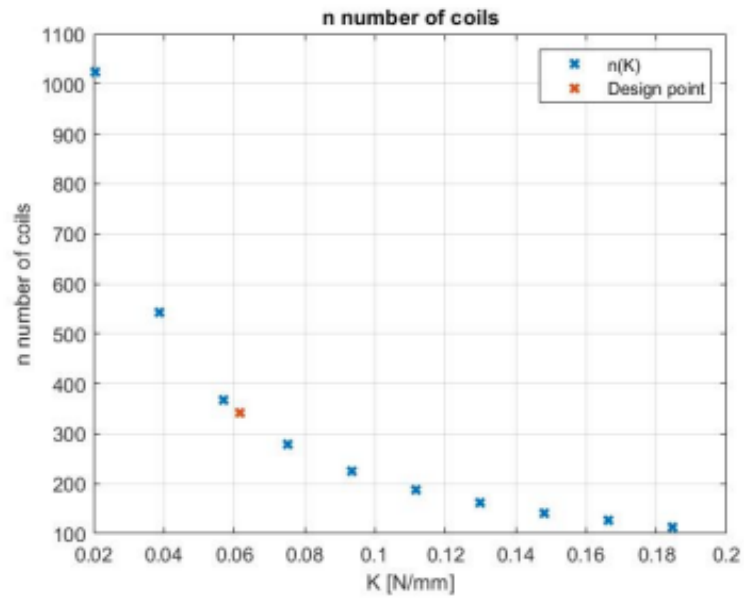


**Figure 4.4:** Number of coils

## 4.3 Horizontal Mover

The horizontal mover is a system designed to direct the tension of the cable to the lowest hook and close to the table surface, onto the gearbox. This system features an oblique pulley anchored on a movable support. The support isn't fixed to the table but is instead anchored on sliding rails. This arrangement allows the oblique pulley to move forward and backward relative to the gearbox, providing a degree of freedom. The system's motion is facilitated by a handwheel fixed on a threaded rod, which passes through the pulley support and screws into a nut embedded in the support. This mechanism converts the screw's rotation into linear displacement of the system.

The mover introduces an additional degree of freedom to the load module. Green arrows in Figure 4.5 illustrate the possible displacements of the oblique pulley. When the motor rotates, the two springs are put under tension and generate equal forces because they experience the same elongation, equivalent to the circumference described by the guide. However, by turning the handwheel of the mover while both springs are tensioned, more or less tension can be applied to one of the springs. Specifically, moving the oblique pulley support away from the gearbox increases spring tension, resulting in a radial force component in addition to the pure torque applied to the gearbox, given by:

$$F_{\text{radial}} = K\Delta x$$

where  $\Delta x$  is the displacement of the mover.

The mover consists of several components:

- Oblique pulley
- Pulley support
- Fixing support
- Linear guides

- Threaded rod and nut
- Fixing screws and bearings

The horizontal mover always operates under traction, with all tensile force being transferred from the cable to the oblique pulley, and then to the support, which ultimately transfers the force to the nut, as depicted in Figure 4.6. While the pulley and its support are free to slide relative to the table surface, the nuts on the fixed support and in the pulley support absorb all forces, maintaining tension on the rod. Rotating the handwheel causes the threaded rod to rotate with respect to the pulley support and nut embedded within it, leading to linear displacement of the oblique pulley. The oblique configuration of the pulley accommodates space constraints, as the braking module is positioned above it.

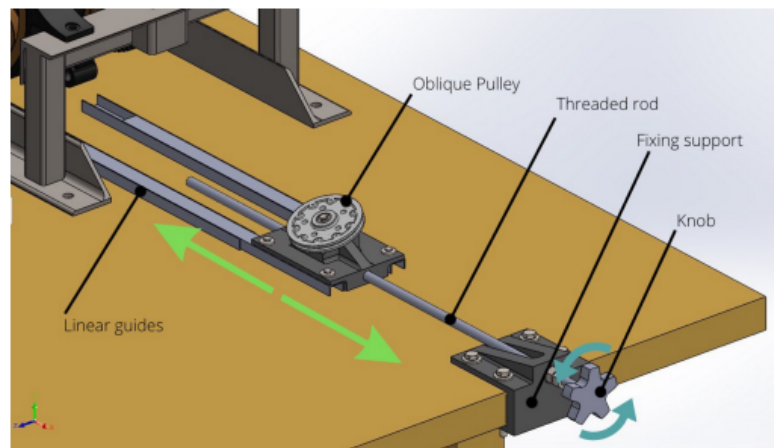


**Figure 4.5:** Horizontal mover architecture (CAD)

## 4.4 Vertical Pulleys System

The vertical pulley assembly is designed to redirect both cables back into the tubes containing the tension springs or the weights incorporated into the system to achieve specific load requirements. Thus, the

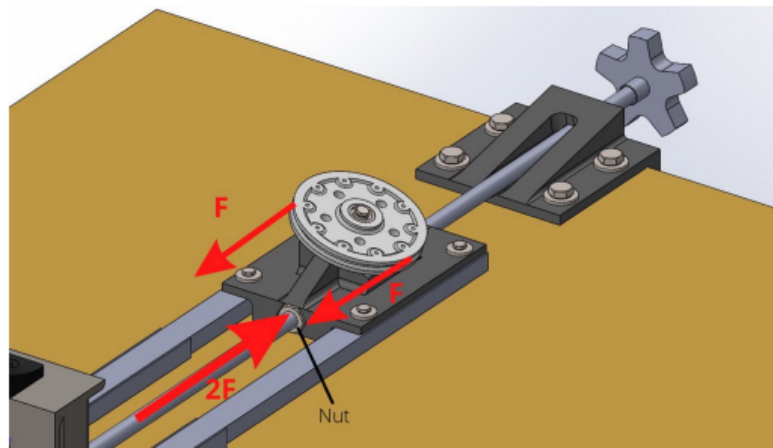


**Figure 4.6:** Forces on oblique pulley support (CAD)

cable from the oblique pulley of the mover and the cable from the top of the rail are rotated 180° and returned inside the tubes.

The system comprises the following elements:

- Aluminum profile
- C-support
- Sliding supports
- Lower return pulley
- Upper return pulley
- Bearings, nuts, and fixing screws

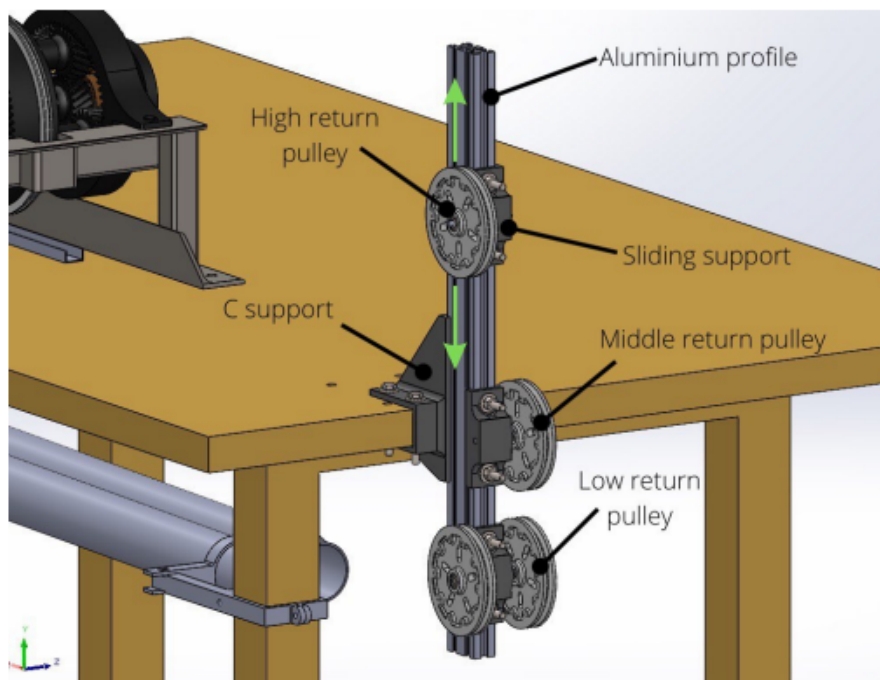


**Figure 4.7:** Vertical pulley system (CAD)

The upper pulley redirects the cable from the top of the rail downward, while the middle pulley redirects the cable from the horizontal mover.

Both cables are then sent back to the lower return pulleys, which guide them back into the tubes containing the springs.

All pulleys are affixed to an aluminum profile via sliding supports. The profile features grooves to accommodate the heads of M6 screws, which secure the sliding supports. This arrangement enables vertical movement of the pulleys. By adjusting the top pulley vertically, over-tensioning can be achieved on one of the springs, inducing a radial force on the gearbox, similar to the horizontal mover. Shielded miniature ball bearings with an outer diameter of 13mm and an inner diameter of 4mm are used on all pulleys to provide better protection from dirt and grease, thus extending their lifespan.

The sliding mounts include a hole to accommodate an M4 threaded rod that supports the pulleys and allows them to rotate. Self-locking nuts are used to prevent the pulleys from unscrewing during rotation. All sliding supports are identical except for the lower one, which supports the two lower pulleys. The axis of rotation of the lower pulleys is tilted  $2^\circ$  from that of the upper pulleys to provide a slight inclination to the tubes containing the springs, preventing interference with the table foot.

All forces exerted by tensioning the cables are absorbed by the pulleys and transferred to the profile, which is attached to the table via the C-support. The C-support is the most structurally stressed component and features ribs both above and below the table surface to support the torque generated by the profile. The system is not automatically in equilibrium, as the force of the upper pulley generates a torque due to its larger arm compared to the other pulleys. This torque is absorbed by the C-shaped support, which has a strengthening rib at the top to reinforce it against the table surface. The profile is attached to the C-support by two M6 screws, one in the top rib and one in the bottom rib, allowing the top rib to absorb loads through compression and the bottom rib through tension.

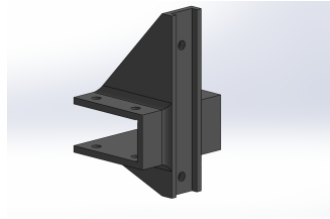


**Figure 4.8:** C-support (CAD)

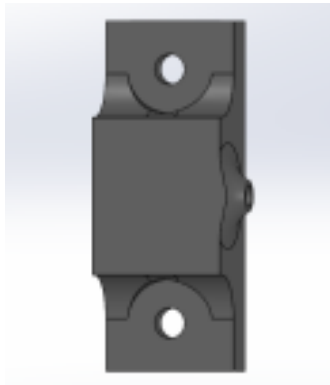


**Figure 4.9:** Sliding support (CAD)

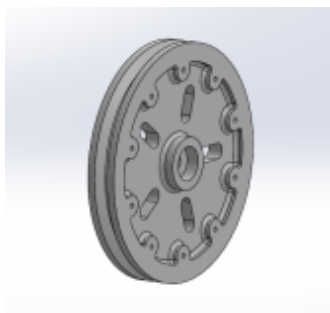


**Figure 4.10:** Pulley (CAD)

## 4.5 Winding guide

The guide is used to allow the cables to wrap neatly around the gearbox as it rotates and the springs are put into traction. The guide consists of two half-circonfereces that were then joined and installed on the gearbox, going to form a circular guide that allows the cables to be wound. The two components were glued to the gearbox surface using cyanoacrylate-based glue. The throat housing the cables was sized by multiplying the diameter of the cables by a factor of 5. Thus given the diameter of the cables equal to 0.8 mm, a throat equal to 4mm was designed. The geometry of the guide is shown in the 4.11. The



**Figure 4.11:** Guide (CAD)

cables used are steel cables which present high resistance at the cost of reducing the elasticity.

## 4.6 Data acquisition system

The acquisition system aims to acquire in real time the load in the form of torque that the load module is applying to the gearbox. The system takes advantage of the use of two loadcells HX711 that constantly measure the tensile force generated by the springs. The torque generated on the gearbox is then calculated as: follows:

$$Torque = (F_1 + F_2) \times r$$

$F_1$  and  $F_2$  are the forces generated by the two springs inside the tubes and  $r$  is the guide radius. Loadcells are powered by 5V drive voltage and are installed on a panel on which the tubes containing the springs are embedded. The panel contains two holes through which cables run that connect each loadcell to its respective spring. In this way the loadcells provide the tensile forces  $F_1$  and  $F_2$  to which the springs are subjected, thanks to 24 high precision A/D converter chip hx711. The loadcells are connected to an Arduino that acquires data and processes it.

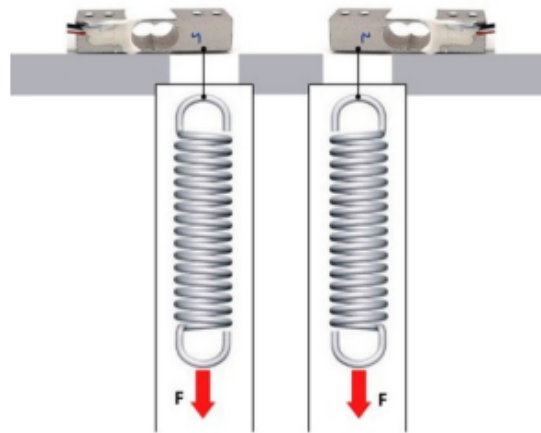


**Figure 4.12:** Data acquisition architecture

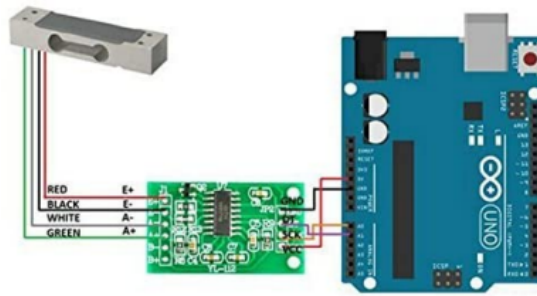


**Figure 4.13:** Data acquisition hardware

# Chapter 5

## Activity Description

The objective of this activity is to accurately compute the compliance ( $k$ ) of the mechanical transmission line and determine its damping characteristics. In order to achieve this, a non-linear model must be tailored to the transmission line of the test bench. This necessitates a thorough study involving a large number of experimental tests.

### 5.1 Experimental Tests

Numerous experimental tests were performed on the test bench, with the the test bench setup detailed in Chapter 4. The testing was conducted according to the following steps:

- Begin data acquisition with no load applied.
- Position the trial weights without allowing them to exert load on the actuator.
- Simultaneously release the weights to impose load on the gearbox.
- Acquire data until the system stabilizes to a steady-state position.

These tests covered a range of load levels from 0.5 kg to 5 kg, allowing for a thorough evaluation of the system's behavior under different loading conditions. For every load level, a total of four tests were conducted, resulting in a comprehensive dataset of forty tests suitable for computational analysis.

## 5.2 Data plotting

The data acquisition system (also described in Chapter 4) generates a .CSV file containing various parameters:

- **Xms**: time
- **C0Drive\_axis\_1r4821**: Encoder position (slow shaft)
- **C1Drive\_axis\_1r4820**: Motor position (fast shaft)
- **Drive\_axis\_1.r62**: Speed setpoint after filter
- **Drive\_axis\_1.r63**: Actual speed smoothed
- **Drive\_axis\_1.r77**: Current setpoint torque-generating
- **Drive\_axis\_1.r76**: Current actual value field-generating
- **Drive\_axis\_1.r1733**: Quadrature-axis voltage setpoint
- **Drive\_control.r722**: Arduino trigger

This data is utilized to plot trends depicting the variations in motor and encoder positions under different loads.

By employing MATLAB functions and scripts, the data is processed and selected to generate the following plots.

## Activity Description

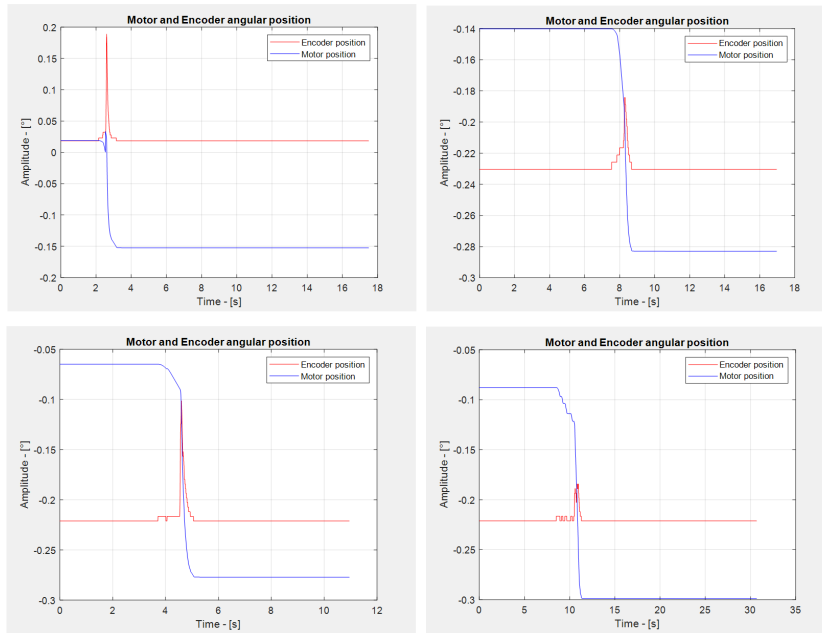


**Figure 5.1:** Data Handling (510g load)

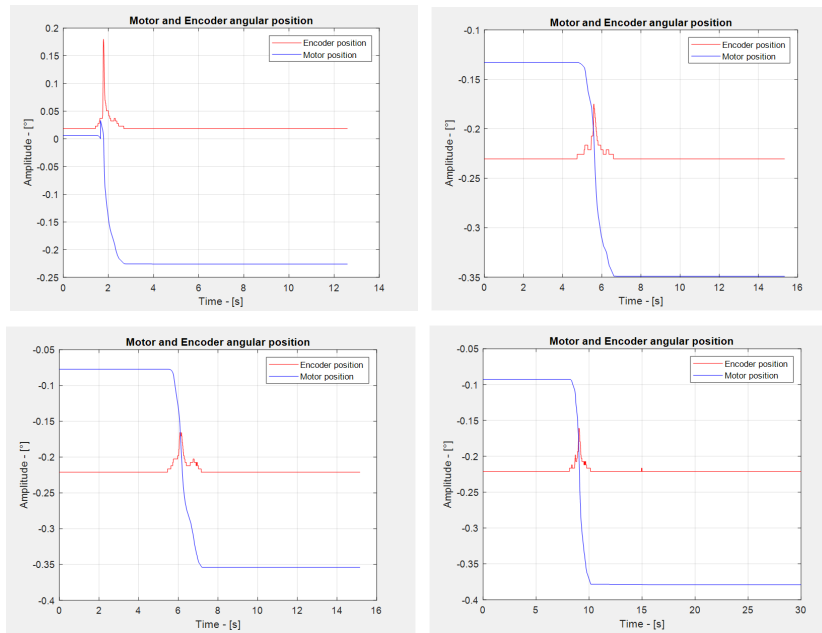


**Figure 5.2:** Data Handling (1000g load)

## Activity Description

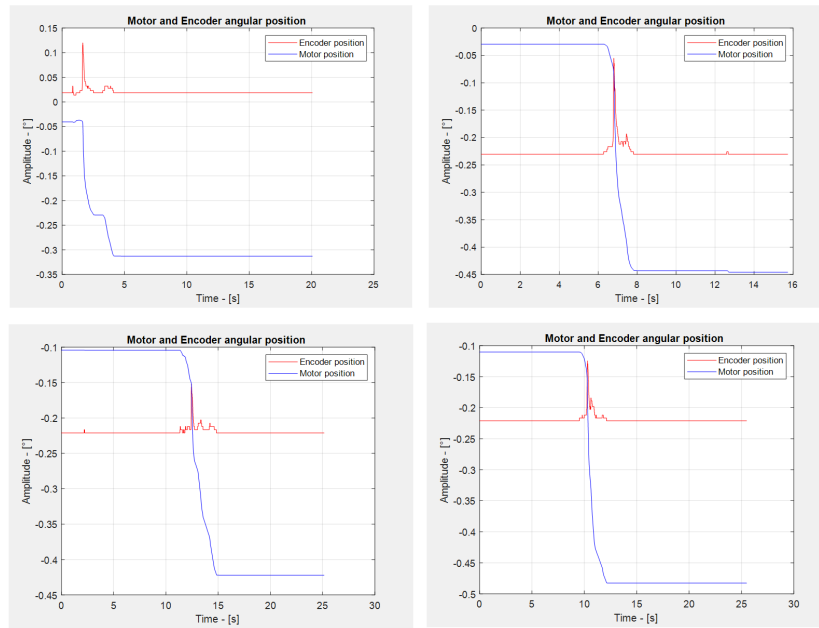


**Figure 5.3:** Data Handling (1510g load)

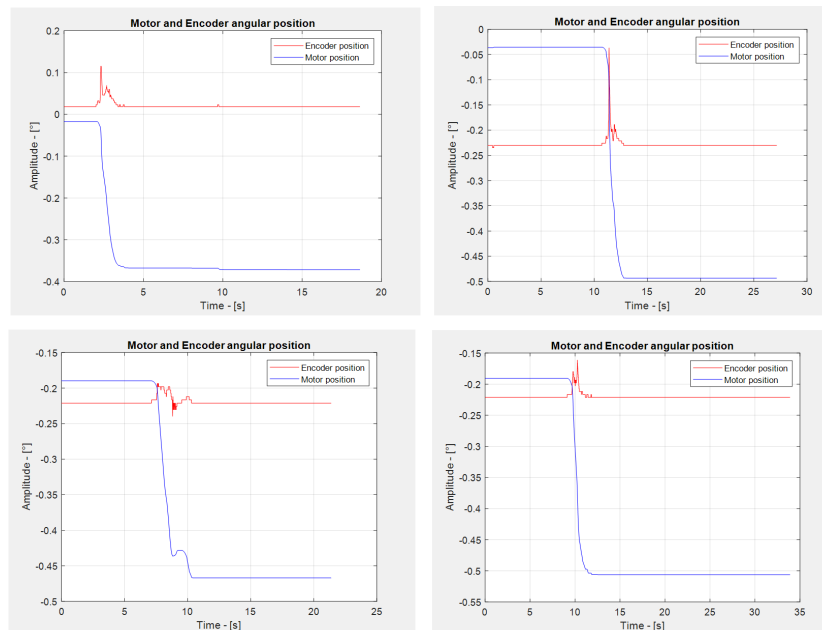


**Figure 5.4:** Data Handling (2010g load)

## Activity Description

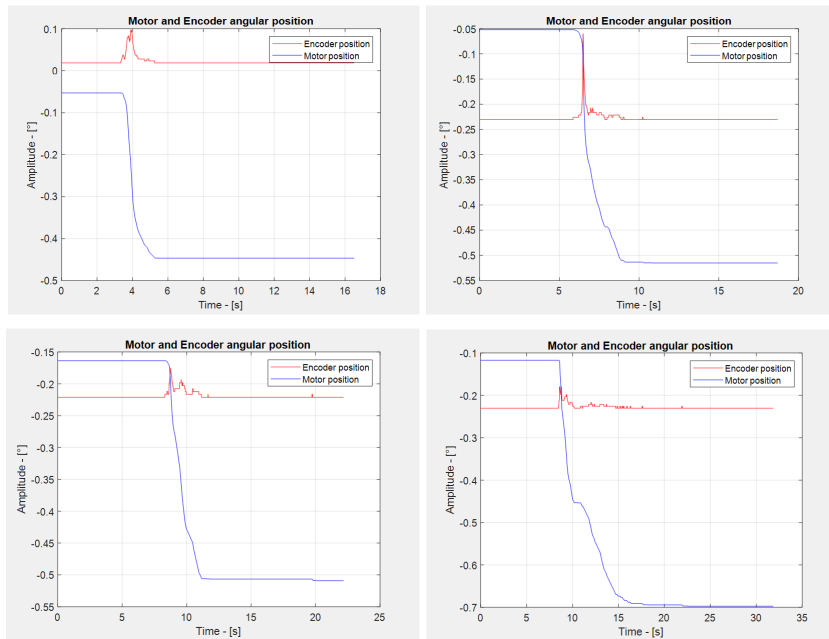


**Figure 5.5:** Data Handling (2520g load)

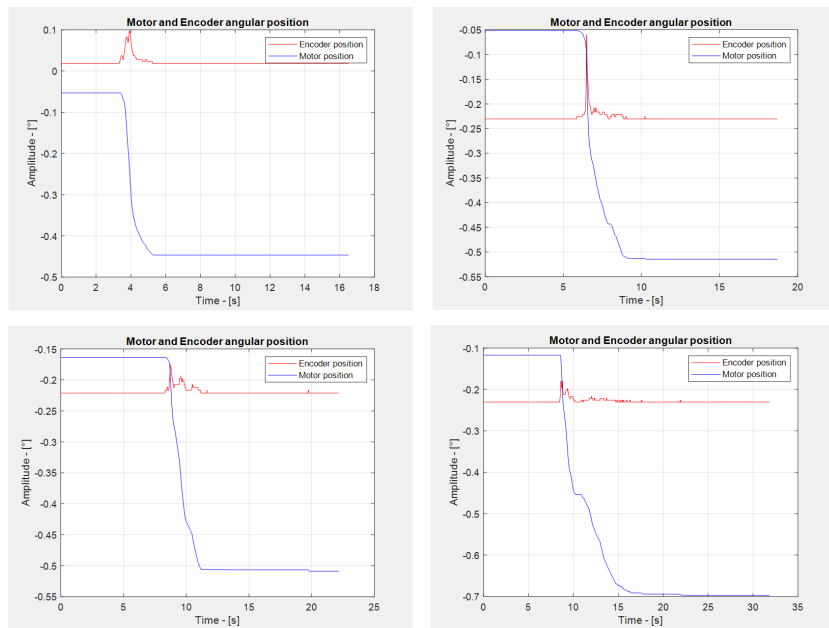


**Figure 5.6:** Data Handling (3020g load)

## Activity Description

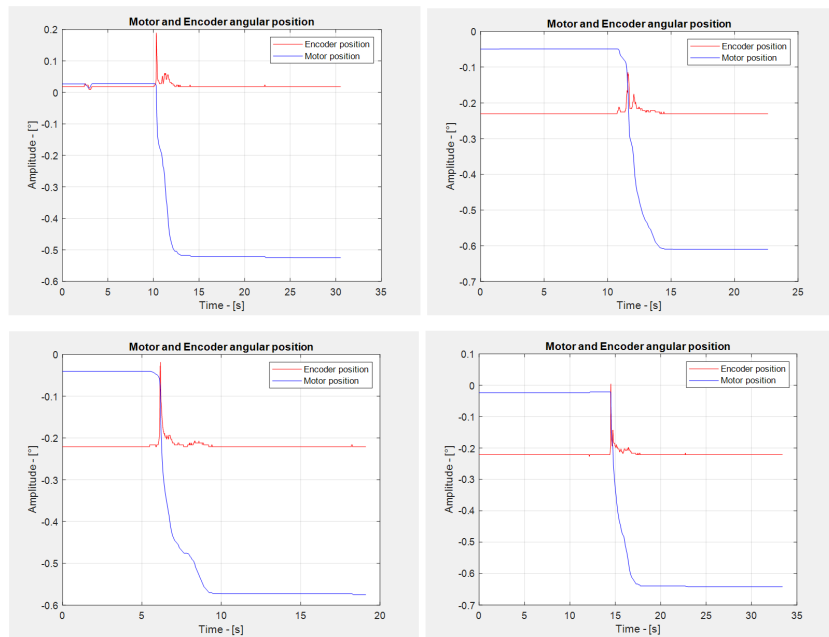


**Figure 5.7:** Data Handling (3533g load)

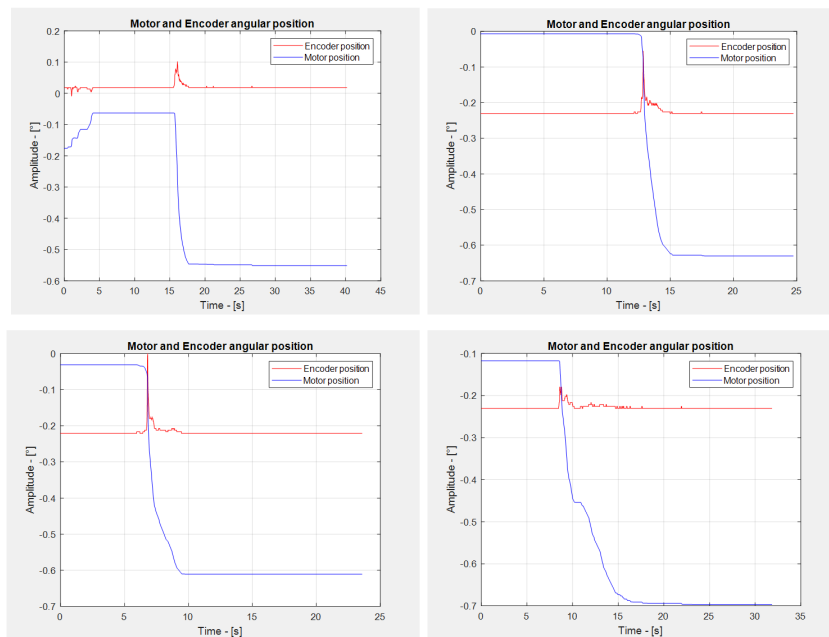


**Figure 5.8:** Data Handling (4031g load)

## Activity Description

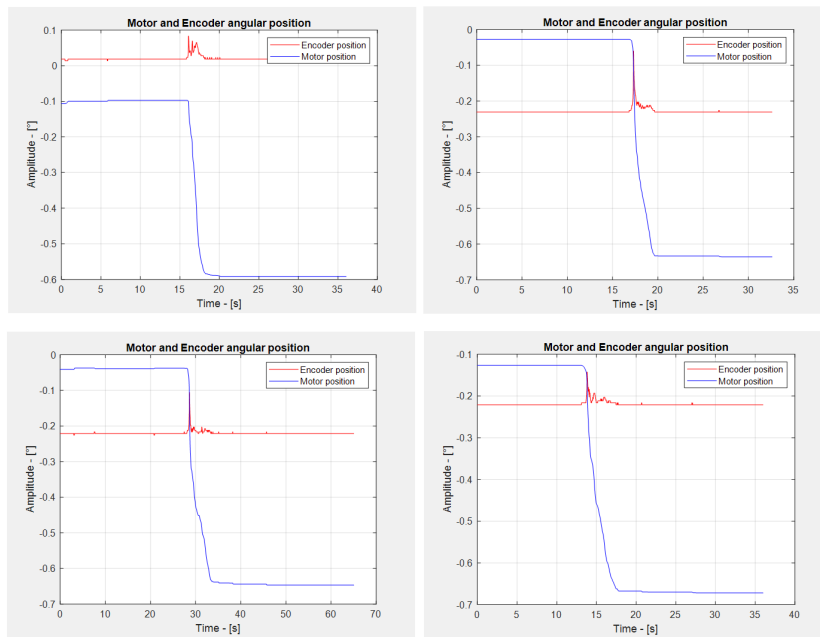


**Figure 5.9:** Data Handling (4541g load)

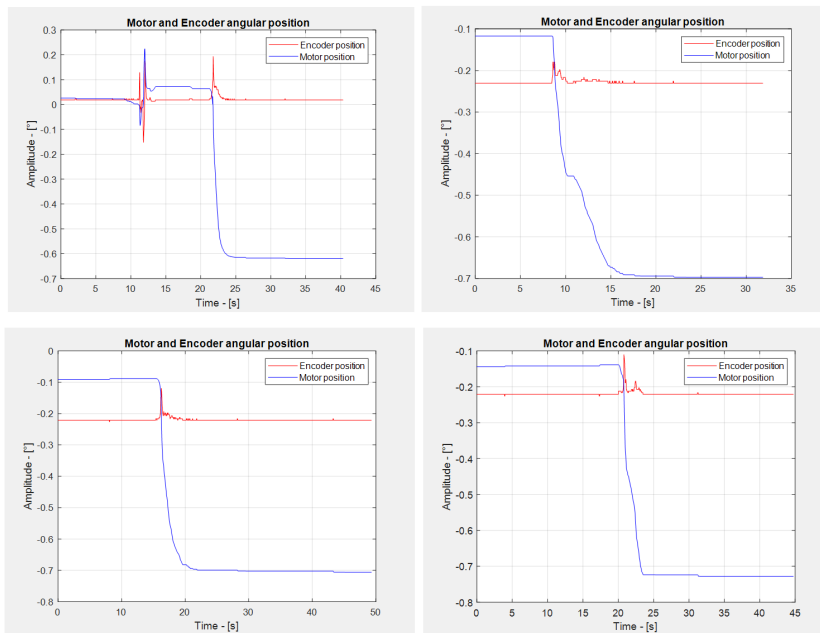


**Figure 5.10:** Data Handling (5042g load)

## 5.3 Computation of the compliance

The final positions of the motor and encoder, along with their corresponding test loads and deltas, are compiled into a table for analysis. This data is then used to plot graphs illustrating the correlation between applied load and angular position. The slope of the curve will provide a semi-accurate estimate of the compliance of the transmission line.

Load [N]	Motor angular position [°]	Encoder angular position [°]	Angular loss [°]
5.09	-0.15245	0.18432	0.33677
5.09	-0.28295	-0.2304	0.052549
5.09	-0.27713	-0.22118	0.052549
5.09	-0.29865	-0.22118	0.077468
10	-0.22578	0.018432	0.244215
10	-0.39911	-0.2304	0.168711
10	-0.35387	-0.22118	0.132682
10	-0.37835	-0.22118	0.157163
15.09	-0.31283	0.018432	0.33126
15.09	-0.44295	-0.2304	0.201086
15.09	-0.42227	-0.22118	0.201086
15.09	-0.48272	-0.22118	0.261535
20.1	-0.36758	0.018432	0.386007
20.1	-0.4936	-0.2304	0.284456
20.1	-0.46701	-0.22118	0.245825
20.1	-0.50627	-0.22118	0.285083
25.2	-0.44061	0.01842	0.459028
25.2	-0.51486	-0.2304	0.284456
25.2	-0.50662	-0.22184	0.284776
25.2	-0.6971	-0.2304	0.466697
30.2	-0.48271	0.018432	0.501142
30.2	-0.55534	-0.2304	0.324941

*Activity Description*

---

30.2	-0.54219	-0.22118	0.321004
30.2	-0.60695	-0.22118	0.385762
35.3	-0.52068	0.018432	0.539112
35.3	-0.2304	-0.61005	0.379654
35.3	-0.22118	-0.57254	0.351356
35.3	-0.22118	0.639573	0.860757
40.3	0.018432	0.546464	0.528032
40.3	-0.62793	-0.2304	0.397531
40.3	-0.22118	-0.61062	0.389438
40.3	-0.2304	-0.69411	0.463709
45.4	0.018432	-0.59159	0.610026
45.4	-0.2304	-0.63317	0.402771
45.4	-0.22118	-0.64377	0.422586
45.4	-0.22118	-0.66996	0.448772
50.4	0.018432	-0.61534	0.63377
50.4	-0.2304	-0.69412	0.463719
50.4	-0.22118	-0.69952	0.478335
50.4	-0.22118	-0.72382	0.502633

**Table 5.1:** Motor and Encoder final positions for every test

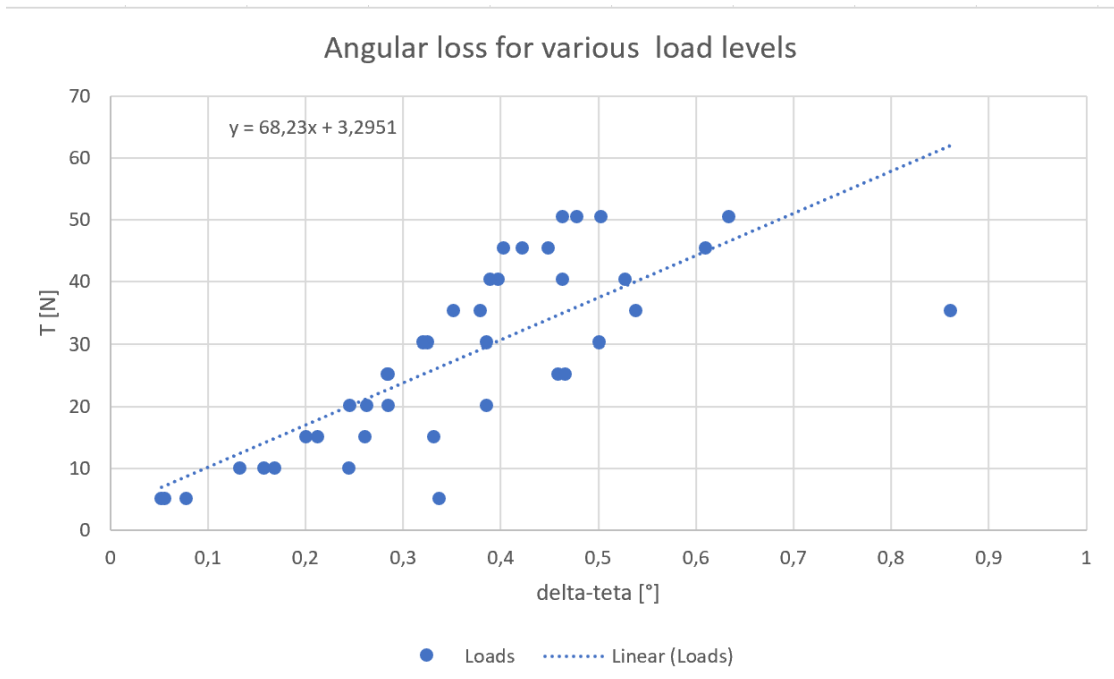


**Figure 5.11:** Angular loss for various load levels

With these results, the compliance value is estimated to be 68.23 Nm/deg.

An estimate for the damping of the system has already been incorporated into the model. Previous research, employing an experimental approach, has identified the predominant contribution of damping in the motor-reductor block. This estimate will serve as an initial approximation, providing insights into the order of magnitude of the damping value. Through iterative fine-tuning, the damping value will be adjusted to accurately represent the entire transmission line.

## 5.4 Implementing the model

The model implemented in Simulink is a closed-loop nonlinear differential equation. It takes torque as input and computes rotational

velocity and angle variation through a series of integrals. These values are then multiplied by the damping and compliance, respectively, and subtracted from the initial load. This model, tailored with compliance data retrieved from experimental tests, is integrated into the wider 'Mechanical Transmission Model' block to simulate transmission line losses in stationary conditions.

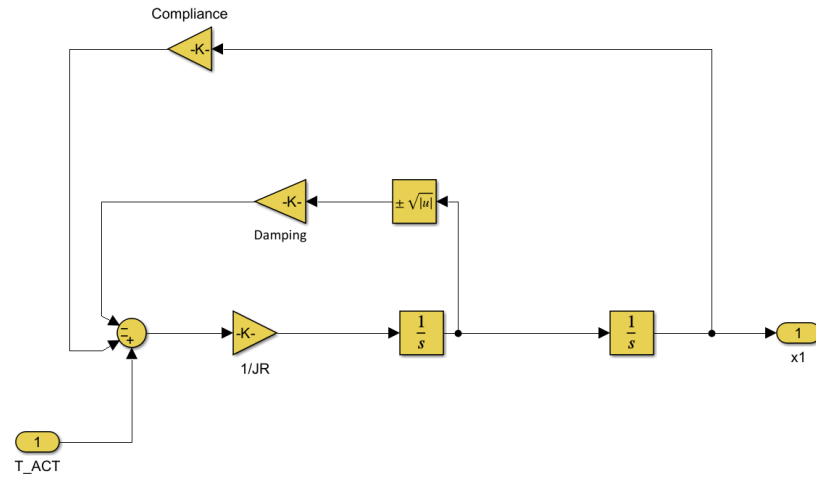


Figure 5.12: Nonlinear model of the losses of the transmission line

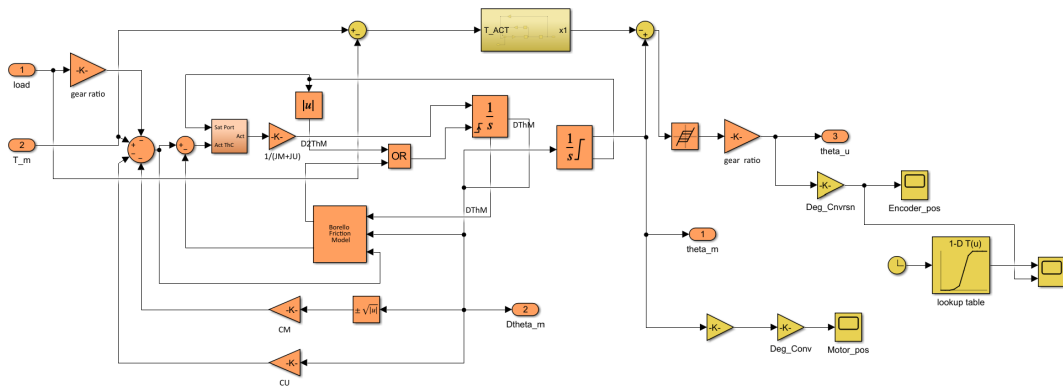


Figure 5.13: Model Integration

# Chapter 6

## Results & Conclusions

### 6.1 Results

After fine-tuning the previously estimated compliance and damping values, significant adjustments were made:

- **Compliance:** Adjusted from 68.23 N/m to 43 N/m.
- **Damping:** Adjusted from 5.5 kg/s to 7.5 kg/s.

These adjustments led to the following results. The figures below compare the position variations of the Encoder and Motor under a 5 kg load, captured from the test bench's data acquisition system (yellow), with the values computed by the implemented model (blue).

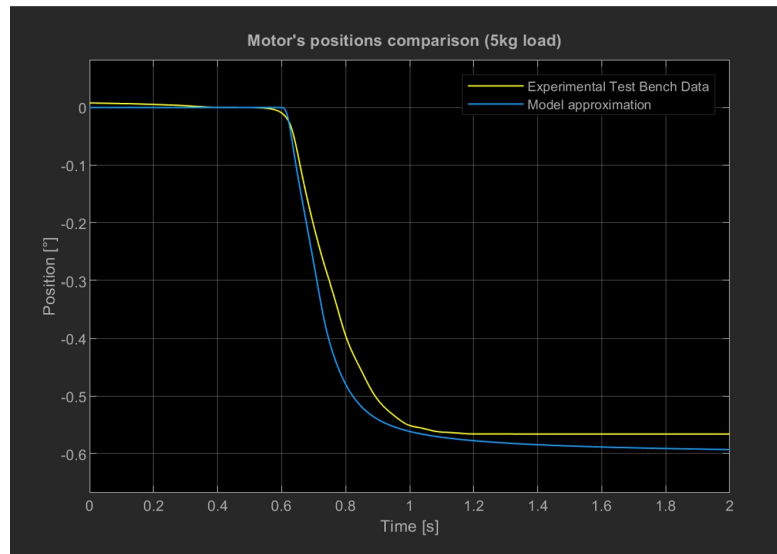


**Figure 6.1:** Comparison of Motor positions between test bench measurements (yellow) and model computations (blue)

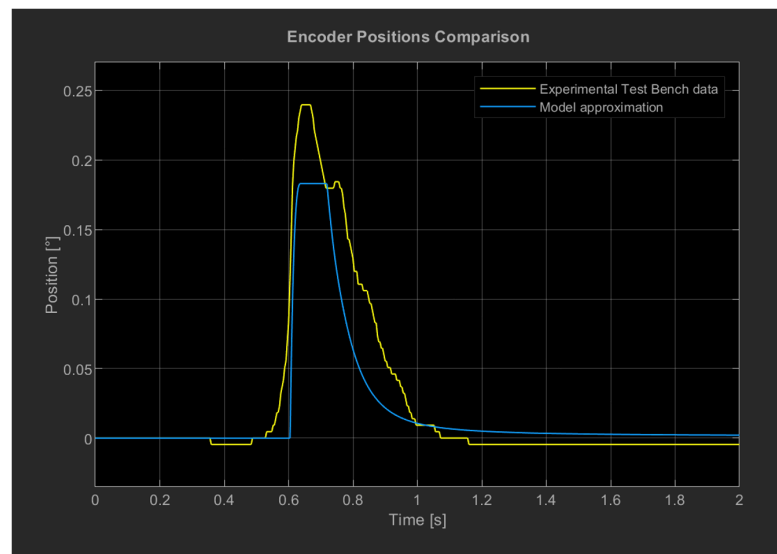


**Figure 6.2:** Comparison of Encoder positions between test bench measurements (yellow) and model computations (blue)

## **6.2 Conclusion**

The iterative refinement process undertaken in this study underscores the importance of empirical validation in fine-tuning complex mechanical systems. Through experimental testing and the implementation of modeling techniques, valuable insights into the compliance and damping characteristics of the transmission line under diverse loads have been acquired. The fine-tuning process of the compliance and damping values demonstrated the validity of our theoretical approach, showing reasonable agreement between model computations and experimental measurements.

The findings presented in this thesis underscore the importance of accurate modeling and analysis in the design and optimization of mechanical transmission systems. By accurately delineating compliance and damping, the predictive capabilities of the models can be enhanced, leading to more effective and reliable system designs.

Looking ahead, the insights gained from this research can be applied to a wide range of applications, from industrial machinery to, most notably, servo-mechanical actuators for aeronautical command transmission lines. By further refining modeling techniques and delving into non-stationary cases, the applicability and accuracy of our models in dynamic scenarios can be heightened. This opens up exciting opportunities for the development of more robust and adaptive mechanical transmission systems, capable of meeting the evolving demands of modern engineering challenges.

In conclusion, advancing our understanding of transmission system dynamics will pave the way for future innovations in the design and optimization of mechanical systems.

## **6.3 Future Developments**

Building upon the groundwork laid by this thesis, future endeavors will prioritize the refinement of modeling techniques and the handling of non-stationary cases. Advanced control algorithms and predictive analytics will be integrated to augment the adaptability and responsiveness of mechanical transmission systems in dynamic operating environments.

Additionally, efforts will be directed towards integrating emerging technologies into the existing modeling framework. By leveraging data-driven approaches, we can improve the accuracy of our models and enable real-time monitoring and optimization of mechanical transmission systems.

Furthermore, research will explore the application of the exposed findings to interdisciplinary fields. By collaborating with experts from diverse disciplines, it would be possible to leverage cross-disciplinary insights to tackle complex engineering challenges and drive innovation in mechanical transmission technology.

Future developments will focus on advancing the state-of-the-art in mechanical transmission systems through the integration of advanced modeling techniques, emerging technologies, and interdisciplinary collaboration.

# Bibliography

- [1] Andrzej Popena, Marek Lis, Marcjan Nowak, and Krzysztof Blecharz. «Mathematical modelling of drive system with an elastic coupling based on formal analogy between the transmission shaft and the electric transmission line». In: *Energies* 13.5 (2020), p. 1181 (cit. on p. i).
- [2] Jianming Li, Zhiyuan Yu, Yuping Huang, and Zhiguo Li. «A review of electromechanical actuation system for more electric aircraft». In: *2016 IEEE International Conference on Aircraft Utility Systems (AUS)*. IEEE. 2016, pp. 490–497 (cit. on p. 1).
- [3] Mary Ellen Roth, Linda M Taylor, and Irving G Hansen. «Status of electrical actuator applications». In: *IECEC 96. Proceedings of the 31st Intersociety Energy Conversion Engineering Conference*. Vol. 1. IEEE. 1996, pp. 191–196 (cit. on p. 1).
- [4] Kai Goebel, George Vachtsevanos, and Marcos E Orchard. *Prognostics*. Tech. rep. SAE, 2013 (cit. on p. 5).
- [5] SIEMENS. *SIMATIC IPC427E Product Information* (cit. on p. 21).
- [6] SIEMENS. *Data sheet for SINAMICS S120 control unit CU310-2PN* (cit. on p. 23).
- [7] SIEMENS. *Data sheet for SINAMICS Power module PM240-2* (cit. on p. 25).

- [8] SIEMENS. *Data sheet for SIMOTICS S-1FK7* (cit. on p. 28).
- [9] Italsensors. *Incremental optical encoders TSW58HS* (cit. on p. 33).
- [10] Pier Carlo Berri, Matteo DL Dalla Vedova, Paolo Maggiore, and Guido Riva. «Design and development of a planetary gearbox for electromechanical actuator test bench through additive manufacturing». In: *Actuators*. Vol. 9. 2. MDPI. 2020, p. 35.
- [11] Matteo Bertone. «Development of an experimental test bench for the validation of prognostic algorithms for electromechanical actuators». PhD thesis. Politecnico di Torino, 2022.
- [12] Francesco Gerbino. «Development and integration of a FBG optical sensor network for prognostics of electromechanical actuators.» PhD thesis. Politecnico di Torino, 2022.
- [13] Guan Qiao, Geng Liu, Zhenghong Shi, Yawen Wang, Shangjun Ma, and Teik C Lim. «A review of electromechanical actuators for More/All Electric aircraft systems». In: *Proceedings of the Institution of Mechanical Engineers, Part C: Journal of Mechanical Engineering Science* 232.22 (2018), pp. 4128–4151.